ADVANCING EARTH AND SPACE SCIENCES

JAMES | Journal of Advances in Modeling Earth Systems®

RESEARCH ARTICLE
10.1029/2025MS005399

**Key Points:**

- Adjoint-based calibration performed against measured velocity data to improve bottom friction estimation for tidal stream energy modeling
- Optimal bottom friction is highly site-specific and limited appropriate calibration data can produce misleading results and overfitting
- Robust validation and calibration data is critical to reduce uncertainty in tidal resource and environmental impact assessments

**Correspondence to:**

C. Jordan,
C.Jordan@ed.ac.uk

**Citation:**

Jordan, C., & Angeloudis, A. (2026). Assimilation of velocity data for tidal hydrodynamics model calibration. *Journal of Advances in Modeling Earth Systems*, *18*, e2025MS005399. https://doi.org/10.1029/2025MS005399

Received 6 AUG 2025
Accepted 21 JUL 2026

**Author Contributions:**

**Conceptualization:** Connor Jordan
**Formal analysis:** Connor Jordan
**Funding acquisition:** Connor Jordan, Athanasios Angeloudis
**Investigation:** Connor Jordan
**Methodology:** Connor Jordan
**Project administration:** Athanasios Angeloudis
**Resources:** Athanasios Angeloudis
**Software:** Connor Jordan
**Supervision:** Athanasios Angeloudis
**Validation:** Connor Jordan
**Visualization:** Connor Jordan
**Writing – original draft:** Connor Jordan
**Writing – review & editing:** Connor Jordan, Athanasios Angeloudis



# Assimilation of Velocity Data for Tidal Hydrodynamics Model Calibration

**Connor Jordan**[1] and **Athanasios Angeloudis**[1]

[1]School of Engineering, Institute for Infrastructure and the Environment, University of Edinburgh, Edinburgh, UK

**Abstract** Assessing tidal stream energy resource typically involves the application of numerical models calibrated against sparse Acoustic Doppler Current Profiler (ADCP) data. This introduces significant challenges in energetic sites which are prone to significant spatiotemporal variations, like the Pentland Firth, Scotland, which is home to the world's highest capacity commercial tidal array. This study investigates the implications of limited calibration data and examines different approaches for constructing an appropriate friction field in tidal hydrodynamics model calibration. We compare performances between models using uniform and sediment-based friction coefficient fields and introduce the first application of adjoint-based calibration for optimizing a resource assessment model based on velocity data. The adjoint approach is applied iteratively and adjusts the friction coefficient with successive ADCP surveys. Our results demonstrate that the most widely applied approach employing a uniform friction coefficient fails to deliver adequate predictive performance across multiple data sets, even at close proximity. In turn, initial adjoint-based calibrations are prone to overfitting, which is rectified only with additional data acquisition. Simultaneously, calibration to solely the channel of interest could lead to significant inaccuracy in kinetic energy fluxes and thus greatly impact upper bound estimates on the resource and array-array interactions. These findings highlight the critical need for extensive and strategic ADCP data collection, which significantly reduces uncertainty and enhances model reliability, advancing the fidelity of coastal ocean models as in the tidal energy application we consider in this study.

**Plain Language Summary** Numerical computer models help engineers estimate the energy available at tidal energy sites, but they need real-world data to be accurate. This data often comes from instruments called Acoustic Doppler Current Profilers (ADCPs), which measure water speed and direction. Many studies use only a few ADCPs and assume the seabed is equally rough everywhere. However, tidal flows can vary greatly across short distances and between tidal cycles, so this "one size fits all" approach can give misleading results. We investigated this at a major tidal turbine site in the Pentland Firth, Scotland. We found that using just a few ADCPs and a single seabed roughness value for modeling can make a model look accurate in one place but fail elsewhere. Because measurements are often collected years apart, this can lead to false estimates of available energy. We tested a more advanced method that allows seabed roughness to vary across the site and added more ADCP data over time. This reduced errors and gave closer predictions to the measured data. Our findings show that developers need well-planned measurement campaigns with enough ADCPs to reduce uncertainty and design efficient, cost-effective tidal energy arrays.

## 1. Introduction

Numerical models are integral components of feasibility studies for tidal stream energy resource assessment and the design of marine energy schemes (Kantha & Clayson, 2000; Kirby, 2016). For coastal ocean models to be reliable, accurate determination on the spatiotemporal evolution of pertinent hydrodynamic quantities (e.g., flow velocity, direction and turbulence levels) are critical (Gunn & Stock-Williams, 2013). However, the cost and complexity of deploying measurement tools for validation such as Acoustic Doppler Current Profilers (ADCPs) at a large scale (Sellar et al., 2018) has proven prohibitive and cumbersome practically.

The lack of comprehensive spatial data coverage through observations leads to the use of computational models. In turn, reliance on models introduces challenges for bounding prediction uncertainties, which must be understood at a distance from areas where validation data is available. ADCPs provide the means to calibrate the data through tuning model inputs, typically consisting of model geometry, tidal boundary forcing, frictional resistance and turbulence parameterization. For the first, availability of bathymetry data in areas of interest has typically improved and acquisition at fine resolution (<1 m) is gradually becoming more accessible. Tidal boundary

**Table 1**
*Selected Numerical Coastal Ocean Model Calibration Studies*

| References | Calibration method | Calibration/validation data | Friction representation |
|---|---|---|---|
| Davies and Aldridge (1993) | Enumeration | Elevation gauges | Uniform |
| Sauvaget et al. (2000) | None[a] | Elevation gauges | Uniform |
| Fernandes et al. (2001) | Enumeration | Elevation gauges | Uniform and variable |
| Gunn and Stock-Williams (2013) | None[a] | Elevation gauges, 4× ADCPs | Uniform |
| Athar et al. (2019) | Enumeration | Elevation gauges | Linear variation across domain width |
| Warder et al. (2021) | Enumeration | Elevation gauges, 1× ADCP | Uniform |
| Ullman and Wilson (1998) | Adjoint | ADCP transects | Independent points scheme |
| Lu and Zhang (2006) | Adjoint | Elevation gauges | Independent points scheme |
| Maßman (2010) | Adjoint | Elevation gauges | N/A |
| Zhang et al. (2011) | Adjoint | Altimetry data, elevation gauges | Independent points scheme |
| Poncot et al. (2017) | Adjoint | Elevation gauges, 1× ADCP | N/A |
| Warder et al. (2020) | Adjoint and Bayesian inference | Elevation gauges | Sedimentological regions |
| Qian et al. (2021) | Adjoint | Altimetry data | Independent points scheme |
| D. Wang et al. (2021) | Adjoint | Altimetry data, elevation gauges | Fully variable |
| Kärnä et al. (2023) | Adjoint | Elevation gauges | Fully variable[b] |
| Mayo et al. (2014) | Kalman filtering | Elevation gauges | Two regions |
| X. Wang et al. (2022) | Time–POD–based coarse incremental parameter estimation[c] | Elevation gauges | Geographic regions |
| Warder et al. (2022) | Bayesian inference | Elevation gauges, 1× ADCP | Sedimentological regions |
| Warder and Piggott (2022) | Bayesian inference | Elevation gauges | Linearly segmented regions |
| Thiébot et al. (2026) | 3DVar data assimilation (with Sobol' screening) | 9× ADCPs | Sedimentological regions |

*Note.* Most studies listed use depth-averaged models and focus on the bottom friction parameter. [a]No calibration results presented. [b]Regularization applied to prevent sharp changes. [c]POD: Proper-orthogonal-decomposition.

forcing is typically informed by global ocean models, whilst turbulence parameterization is often linked to the type of model used and computational resource. In site-focussed coastal ocean models (e.g., in the consideration of a particular area for a marine energy technology deployment), the sea-bed roughness coefficient is often the dominant parameter used for model tuning. Invariably, this accounts for broader physical and numerical dissipation processes which are either not included in the model equations solved or are resolved in a simplified manner that filters the complex heterogeneity of certain flow structures in the coastal ocean (Mackie et al., 2021).

In improving prediction agreement against scattered validation points, several methods have been applied to calibrate models through a parameterised drag term (Table 1). The simplest technique is to enumerate through a set of uniform friction parameter values, which can be automated by techniques such as Bayesian inference. To further improve agreement across a wider domain, it is likely that a spatially varying field is necessary, as discussed in detail in Appendix A. This can range from linear segmentation of the domain to enabling full variation at every node on the mesh of the discretised domain. For limited control parameters, a surrogate representation of the model can be used in conjunction with techniques such as Kalman filtering (e.g., Mayo et al., 2014). Otherwise, for increased freedom an adjoint approach may be deployed (e.g., Kärnä et al., 2023). Considering the relevant studies in Table 1, almost all rely on tide elevation gauges or satellite altimetry with several focussed on a global scale (e.g., X. Wang et al., 2022). For such a scope, spatial variation is a function of both localised features and the widely changing channel dynamics.

Thiébot et al. (2026) provides an exception whereby current data has recently been obtained for a highly energetic site subject to a tidal stream energy development. For such projects, smaller scales, that is $<\mathcal{O}(10^2)$ m, become critical in addressing engineering problems such as the optimal layout of turbines at a complex site. Given the direct relationship of array performance with the propagation of tidal kinetic energy, calibration must extend beyond elevation predictions to accurately capture velocity magnitude and direction (Gunn & Stock-Williams, 2013). It has been observed that within an individual array site there is substantial spatiotemporal variation (Warder et al., 2021) and wake interaction is critical in obtaining an optimal layout of devices (Jordan et al., 2022). With commercial arrays imminent (Department for Energy Security and Net Zero, 2023), micro-siting procedures will require accurate velocity directions, to understand extractable yield potential as opposed to estimating kinetic energy (Jordan et al., 2023). By extension, other quantities such as volumetric fluxes are important to understand regional- and array-scale blockage effects (see Vennell et al., 2015) and therefore define the upper-bound on energy extraction (Garrett & Cummins, 2008).

In this context, international standards such as IEC TS 62600-201 (International Electrotechnical Commission, 2025) provide guidance on tidal resource assessment, which necessitates that annual energy production (AEP) shall be assessed by hydrodynamic modeling for complex large scale sites (Cl. 5.2). Model calibration through bottom friction and turbulence parameter adjustment is recommended (Cl. 7.5.2), albeit with loose guidance due to the early stages of understanding of dynamic sites and availability of accompanying data. These guidelines are therefore often applied in data-limited environments, where the number and distribution of ADCP measurements are constrained (Ramos & Ringwood, 2016). The present study examines how the availability and spatial distribution of calibration data influence model accuracy, providing insight into the sensitivity of resource estimates under conditions consistent with practical deployments.

Reflecting on this, we exploit a series of ADCP deployments over multiple time periods within close proximity that is within $\mathcal{O}(10^0) - \mathcal{O}(10^2)$ m, accumulated over the early stages of development of an operational tidal array. Through an adjoint-based calibration technique, we investigate the sensitivity of numerical model accuracy to the number of calibration stations available and the impact that this may have on tidal resource assessment and site design.

## 2. Methodology

Sections 2.1–2.3 describe the hydrodynamics model and outline how its calibration to ADCP data is performed, whilst Section 2.4 sets out the subsequent research design. Section 3 provides information on the case study area that the methodology will be applied to.

### 2.1. Shallow Water Equation Modeling in *Thetis*

*Thetis* (Kärnä et al., 2018) utilizes *Firedrake* (Ham et al., 2023; Rathgeber et al., 2016) to solve partial differential equations using the finite element method. *Thetis* is applied in its depth-averaged configuration, solving the non-conservative form of the non-linear shallow-water equations,

$$\frac{\partial \eta}{\partial t} + \nabla \cdot (H_d \mathbf{u}) = 0, \tag{1}$$

$$\frac{\partial \mathbf{u}}{\partial t} + \mathbf{u} \cdot \nabla \mathbf{u} + g \nabla \eta + f \mathbf{u}^{\perp} = \nabla \cdot \left(\nu \left(\nabla \mathbf{u} + \nabla \mathbf{u}^T\right)\right) - \frac{\boldsymbol{\tau_b}}{\rho H_d}, \tag{2}$$

where $\eta$ is the water elevation, $H_d$ is the total water depth, $\mathbf{u}$ is the depth-averaged velocity vector, and $\nu$ is the horizontal eddy viscosity. The term $f\mathbf{u}^{\perp}$ represents the Coriolis "force," $\mathbf{u}^{\perp}$ is the velocity vector rotated counter-clockwise over 90°, and $f = 2\Omega \sin(\zeta)$ with $\Omega$ the angular frequency of the Earth's rotation and $\zeta$ the latitude. The bed shear-stress ($\tau_b$) effects are represented through the Manning's $n_M$ formulation as per Mackie et al. (2021):

$$\frac{\boldsymbol{\tau_b}}{\rho} = g n_M^2 \frac{|\mathbf{u}|\mathbf{u}}{H_d^{\frac{1}{3}}}, \tag{3}$$

The treatment of inter-tidal processes, discretization and time-marching are applied consistently to Jordan et al. (2022).

### 2.2. Adjoint-Based Data Assimilation Technique

Where calibration is performed using ADCP data, adjoint-based optimisation is deployed to determine the spatially varying bed friction, in this case through the $n_M$ coefficient of Equation 3. The inverse of the "forward" *Thetis* model is being determined, to minimize a cost function, $J$. Following the notation of Kärnä et al. (2023), $\mathcal{F}$ describes the forward operator over the entire simulation and consists of non-linear solves, time-marching to obtain the solutions of Equations 1 and 2. The vector $\mathbf{Q}$ is an aggregation of the model state, $\mathbf{q}$, over $N$ timesteps (that is, $\mathbf{Q} = \left(\mathbf{q}^0, \ldots, \mathbf{q}^N\right)$ such that the forward operator is expressed as:

$$\mathcal{F}(\mathbf{Q}) = 0 \tag{4}$$

This simplifies notation and is evaluated by running the full forward model. The linearized forward operator is denoted as $\tilde{\mathcal{F}}$, required for the efficient calculation of the adjoint equations. The general optimisation problem can be posed based on an unknown value or distribution of a control parameter(s), denoted as $\boldsymbol{\theta}$ in Kärnä et al. (2023). The forward operator can thus be expressed as $\mathcal{F} = \mathcal{F}(\mathbf{Q}, \boldsymbol{\theta})$. In this study, the control parameter, $\boldsymbol{\theta}$, is the spatially varying Manning coefficient field, $n_M$, and so the inverse optimisation problem is given by:

$$\min_{\mathbf{Q}, n_M} J\left(\mathbf{Q}, n_M\right), \quad \text{subject to } \mathcal{F}(\mathbf{Q}, n_M) = 0. \tag{5}$$

Assuming that $J$ is differentiable, and using the notation of Funke (2013) ($\mathbf{Q}$ and $n_M$ are expressed as column vectors and the partial derivatives of a scalar, e.g., $\partial J / \partial \mathbf{Q}$, are row vectors), the gradient can be defined,

$$\frac{dJ}{dn_M} = \frac{\partial J}{\partial \mathbf{Q}} \frac{d\mathbf{Q}}{dn_M} + \frac{\partial J}{\partial n_M}. \tag{6}$$

The final term can be directly determined through symbolic differentiation. The first term of the right-hand side is computed from the discrete adjoint equation,

$$\left[\frac{\partial \tilde{\mathcal{F}}}{\partial \mathbf{Q}}\right]^T \mathbf{L} = \left[\frac{\partial J}{\partial \mathbf{Q}}\right]^T, \tag{7}$$

where $\mathbf{L} = \left(\lambda^0, \lambda^1, \ldots, \lambda^N\right)$ is the time-agglomerated adjoint variable. The adjoint variable and model states share the same shape, that is, for each $\eta^n$ and $\mathbf{u}^n$ pair, there exists a corresponding adjoint field $\lambda^n$. Equation 7 is solved backward in time as the transpose operation effectively reverses the temporal direction. This yields the computation of $\frac{dJ}{dn_M}$ through:

$$\frac{dJ}{dn_M} = -\mathbf{L}^T \frac{\partial \tilde{\mathcal{F}}}{\partial n_M} + \frac{\partial J}{\partial n_M}. \tag{8}$$

The *pyadjoint* package is used to enable automatic derivation of the adjoint equation by differentiating the forward equations (Farrell et al., 2013; Mitusch et al., 2019). A similar approach can then be implemented to determine $\partial \tilde{\mathcal{F}} / \partial n_M$ and $\partial J / \partial n_M$. For more details, (Kärnä et al., 2023) expands on the implementation in the *pyadjoint* package. This entails running *Thetis* to obtain the forward solve operations and model state before reversing the temporal direction and applying the linearized adjoint operators, enabling evaluation of $\frac{dJ}{dn_M}$.

### 2.3. Velocity Data-Driven Optimisation

Unlike the adjoint-based studies of Table 1, we minimize the loss, $J$, between modeled and observed velocity signals, rather than elevation data. We let $\mathbf{u}^o_{i,n}$, $\mathbf{u}^m_{i,n}$, for $i = 1, \ldots, B$ and $n = 1, \ldots, N$, denote velocities at $B$ ADCP deployment locations, where superscripts $o$ and $m$ denote observed and modeled values, respectively.

The misfit is computed based on the magnitude of the velocities, $|\mathbf{u}|$. As the magnitude is dependent on both velocity components (eastward and northward), we expect the direction to implicitly be tuned despite not being explicitly formulated in the loss function. The total misfit for each ADCP is weighted by the inverse variance of

**Table 2**
*ADCP Data Durations and Calibration Periods*

| | ID | Start date | End date | Duration (days) | Calibration period |
|---|---|---|---|---|---|
| Inner Sound | 2013-ERI | 17/02/2013 | 20/03/2017 | 32 | 2013–02 |
| | 2013-EXE | 19/02/2013 | 22/03/2013 | 32 | 2013–02 |
| | 2017-2 | 03/08/2017 | 29/08/2017 | 27 | 2017–08 (a) |
| | 2017-3 | 02/08/2017 | 29/08/2017 | 28 | 2017–08 (a) |
| | 2017-4 | 15/10/2017 | 12/12/2017 | 59 | 2017–10 (b) |
| | 2022 | 20/10/2022 | 30/11/2022 | 42 | 2022 |
| Outer Sound | 2001-C1 | 15/09/2001 | 14/10/2001 | 30 | 2001 |
| | 2001-C2 | 19/09/2001 | 20/10/2001 | 32 | 2001 |
| | 2001-C3 | 18/09/2001 | 14/10/2001 | 27 | 2001 |

the observed velocities to account for different variability at each location. The variance of the observed velocities at each station is given by:

$$(\sigma_{o,i})^2 = \frac{1}{N}\sum_{n=1}^{N} |\mathbf{u}^o_{i,n}|^2,$$

and the cost function $J_\sigma$ is computed as

$$J_\sigma(\mathbf{Q}, n_M) = \frac{1}{B}\sum_{i=1}^{B}\frac{1}{(\sigma_{o,i})^2}\sum_{n=1}^{N}(|\mathbf{u}^m_{i,n}| - |\mathbf{u}^o_{i,n}|)^2.$$

Applying inverse-variance scaling to the velocities helps ensure that no single station disproportionately influences the optimisation problem.

The optimisation problem (Equation 5) is solved with the limited-memory Broyden-Fletcher-Goldfarb-Shanno (L-BFGS-B) quasi-Newton method with bound constraints (Byrd et al., 1995) from the SciPy package (Virtanen et al., 2020). During the iteration, we impose lower and upper bounds, 0.025 and 0.1 s m$^{-1/3}$, respectively, for the Manning coefficient $n_M$ field.

## 2.4. Numerical Experiment Design

### 2.4.1. Benchmark Cases

#### *2.4.1.1. Uniform Friction Coefficient*

The most common approach for the bottom friction in the context of resource assessment (see Table B1) is to apply a uniform coefficient. This is particularly likely in 3D models, where large scale models are substantially higher in computational time and memory costs, making spatially varying calibration challenging (see e.g., Ramos & Ringwood, 2016). In defining the best value, we iterate through a set of uniform parameters and present the best performing value of uniform Manning.

#### *2.4.1.2. Sedimentological Mapping*

An alternative approach is to use a variable friction coefficient, $n_M$, that is related to the seabed particle size, as in Mackie et al. (2021) and Guillou and Thiébot (2016). To calibrate the model on this basis, we first determine a $n_M$ distribution by use of data from the British Geological Society (2020). This data set provides sea-bed descriptions only, leading to large variation in potential particle size to use in estimation of friction parameters. We determine the range of particle sizes possible for each sediment type. To map from the bed particle size, $d$, to $n_M$ we use the relationship by Strickler (1923),

$$n_M = \frac{d_{50}^{1/6}}{C}, \tag{9}$$

where $d_{50}$ is the median grain size. $C$ is the calibration factor, which can act non-uniformly over the field. We use a uniform value of $C = 21.1$, as published originally by Strickler (1923) in the context of fixed boundary, gravel river beds. We present the results only for the best performing case between the use of the minimum, average and maximum particle sizes.

### 2.4.2. Adjoint-Based Parameter Estimation

The adjoint-based approach discussed in Sections 2.2 and 2.3 is deployed for a series of tests.

Firstly, the minimum calibration period required is determined through a series of calibrations for each time period that ADCP data is available. This is done as a straightforward sensitivity analysis where the number of flood-ebb cycles used is gradually increased until no further improvement in model performance is derived.

Following this step, the model is calibrated multiple times in an "online data assimilation" fashion to sequentially embed our increasing knowledge of the system into the model as new data becomes available. This emulates the process that might be carried out by a modeler acting on behalf of an array developer. Accordingly, the model is initially calibrated for the oldest ADCP data set obtained. As more data is obtained, the model is iteratively re-calibrated, using a subset of sampling intervals from ADCP data sets. For ADCP data sets, specific details and considerations are expanded in Section 3.

## 3. Orkney Isles Simulation

Our case study area is within the Orkney archipelago, the domain for various upcoming tidal stream energy projects. The Inner Sound of the Pentland Firth is home to the MeyGen project (https://ampeak.energy/tidal-stream/meygen/), currently consisting of 4 × 1.5 MW capacity devices. As of 2025, UK Government support is in place for expansion to over 50 MW and lease allowance exists for 398 MW of rated capacity.

### 3.1. Model Discretization and Geometry

The model discretization adopts an unstructured format of triangular elements, using the *qmesh* package (Avdis et al., 2018). The mesh designed is refined to 300 m in the main portion of the Pentland Firth, with 100 m resolution at the south of Stroma and Northeast Scottish mainland. In the Inner Sound, the mesh is further resolved to 50 m within the MeyGen lease area which serves as our area of interest. The mesh tested within the study consists of 20,715 vertices and 37,718 elements and is presented in Figure 1 demonstrating the varying resolution across the domain.

The model bathymetry data is described in Jordan and Angeloudis (2025) and combines data sets from Edina Digimap Service (2020) for the broader coverage of the domain, MeyGen Ltd high-resolution surveys at the Inner Sound and GEBCO (2015) to in-fill any remaining regions.

For previous studies, a uniform value of 1 $m^2\ s^{-1}$ has been used for the horizontal eddy viscosity (Jordan et al., 2022). This is increased to 5 $m^2\ s^{-1}$ following a sensitivity analysis with more details expanded later in Section 5.1.

### 3.2. Model Boundary and Initial Conditions

The open sea boundaries are forced using the Q1, O1, P1, K1, N2, M2, S2, and K2 tidal constituents from the TPXO08 database (Egbert & Erofeeva, 2002). For advancing the model in time an implicit backward difference is used with a timestep, $\Delta t = 300$s. Appropriate spin-up time for a coastal ocean model depends on the purpose of the model. For coastal ocean models that focus on tidal energy, this duration is typically 24–48 hr (e.g., Adcock et al. (2013)). Comparisons against measured data here infers this as appropriate and sensitivity checks indicate that for the friction parameter values anticipated for the model, a single day of spin-up time would be sufficient.

Rather than ramping up the simulation from an equilibrium state with a gradual increase in boundary forcings, we use an initial state generated from a case that used a uniform Manning coefficient $n_M$. Specifically, we use the

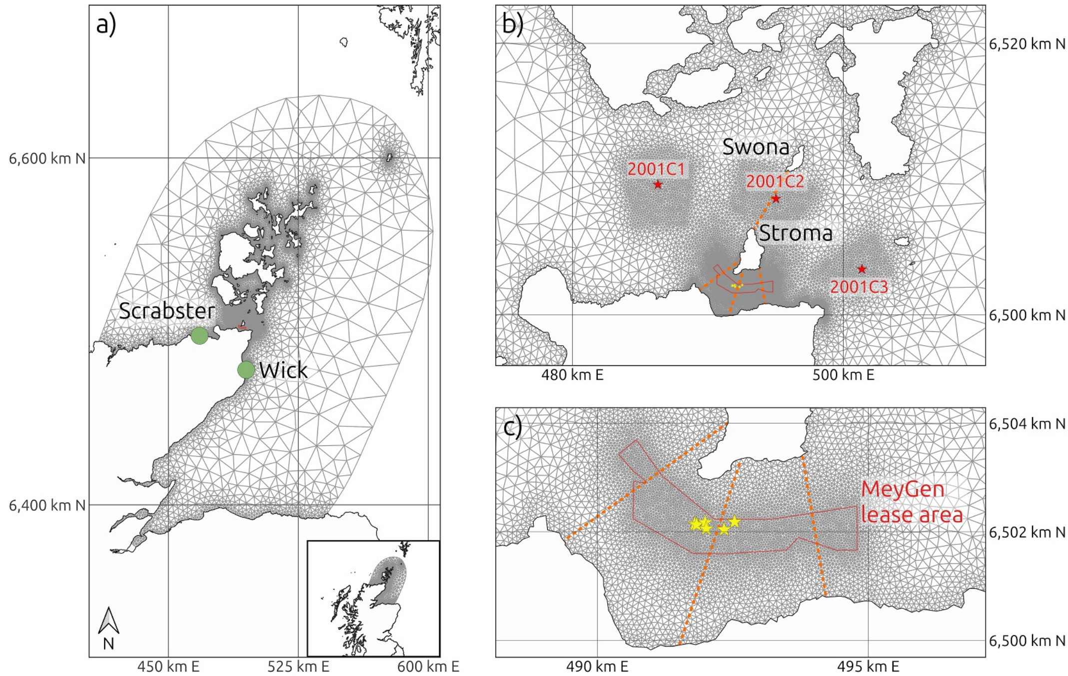


**Figure 1.** Mesh for the computational domain of the Pentland Firth, with subfigures progressively showing the area of interest. The green dots in (a) highlight the location of two tide gauges. In (b), Stroma and Swona are labeled, two islands that split the Pentland Firth into channels. The positions of 3 ADCPs deployed in the Outer Sound are also shown. The red line in (c) indicates the area of the Inner Sound leased for the development of the array and the primary ADCP locations used for calibration are marked with yellow stars. These are shown in more detail in Figure 2. Orange dashed lines indicate flow transects. Projection: UTM Zone 30N.

optimal parameter that has been found for the uniform friction coefficient approach described in Section 2.4.1.1. We then allow one day at full forcing for the model to adapt to the new Manning field. This follows Kärnä et al. (2023), where it was noted that a realistic initial guess is important for the optimisation procedure.

### 3.3. Calibration and Validation Data

#### 3.3.1. Tide Gauges

Given the free surface elevation time series at regional stations through the UK tide gauge network, harmonic analysis is conducted to derive individual tide constituents (Pugh & Woodworth, 2014). This was carried out using the *Python* library *uptide* to perform a least squares regression on $\eta(t)$ to determine amplitude $H_{B,c}$ and phase $\phi_{B,c}$ of individual tidal constituents $c$ at a station $B$. Nearby gauges at Wick and Scrabster are used, as shown in Figure 1. This data is used only for validation and is not assimilated.

#### 3.3.2. Acoustic Doppler Current Profilers

Several ADCP deployments have been undertaken at the MeyGen site. Table 2 lists the ADCP survey data used in this study. An expanded version is provided in Appendix C, with supporting comments on the data quality of each sampling campaign. The data provided was processed from the raw ADCP format with quality control performed to remove significant spikes and spurious entries in the data. Further post-processing was still required for most ADCPs to remove data entries in the surface side-lobe interference zone. Similarly, some ADCPs required data from the blanking zone to be removed and a velocity profile was fitted to in-fill missing data to avoid over-estimating the velocity when depth-averaged. Even so, the current speed data remains mostly unchanged in post-processing of the data. For direction, a vessel mounted survey covering 14 locations was used to estimate corrections for compass errors as discussed in Appendix C.

Additional ADCPs from the Outer Sound have also been made available for comparison as shown in Figure 1 (Easton et al., 2012). These are not initially included as part of the assimilation study and are instead used to

**Table 3**
*Duration Sensitivity Study Validation Results for $\mathcal{R}_{speed}$*

| | Number of flood/ebb cycles used for training | | | | | | | | | |
|---|---|---|---|---|---|---|---|---|---|---|
| | 1 | | 2 | | 3 | | 4 | | 7 | |
| Station | Ebb | Flood | Ebb | Flood | Ebb | Flood | Ebb | Flood | Ebb | Flood |
| 2013-ERI | 93.40 | 92.60 | 93.60 | 92.10 | 93.80 | 92.85 | 93.95 | 92.95 | 94.15 | 92.35 |
| 2013-EXE | 93.35 | 94.20 | 93.65 | 94.05 | 93.90 | 94.20 | 93.85 | 94.40 | 94.00 | 94.40 |
| 2017-2 | 94.00 | 95.70 | 94.60 | 96.00 | 94.20 | 96.05 | 94.10 | 96.00 | 94.50 | 96.25 |
| 2017-3 | 93.15 | 95.30 | 92.80 | 95.20 | 92.55 | 95.50 | 92.60 | 95.30 | 92.05 | 95.70 |
| 2017-4 | 88.95 | 91.35 | 89.25 | 91.35 | 90.20 | 91.20 | 90.50 | 91.70 | 90.50 | 91.55 |
| 2022 | 90.50 | 91.50 | 92.55 | 92.20 | 91.65 | 92.45 | 91.40 | 92.20 | 92.15 | 92.40 |
| **Tide Averages** | 92.22 | 93.44 | 92.74 | 93.48 | 92.72 | 93.71 | 92.73 | 93.76 | 92.89 | 93.77 |
| Relative Change | +0.00% | +0.00% | +0.56% | +0.04% | +0.54% | +0.29% | +0.55% | +0.34% | +0.73% | +0.35% |
| **Combined Average** | 92.83 | | 93.11 | | 93.21 | | 93.25 | | 93.33 | |
| Relative Change | +0.00% | | +0.30% | | +0.41% | | +0.45% | | +0.54% | |

*Note.* Four sets of calibrations are performed with an increasing number of cycles. The 2013 and first two 2017 ADCP stations are combined as deployment periods overlap, returning results for when calibrating for both multiple and single ADCPs.

provide an indication of how the model performs in a neighboring channel. These are later included in the assimilation process once the Inner Sound has been investigated in isolation.

For the adjoint-based calibration, as part of the "online" assimilation approach, depth-averaged velocities are extrapolated to a single time period. This is done in two steps:

1. An adjoint-based calibration is carried out for each single ADCP (as outlined in Section 2). This generates a friction map intentionally overfit for the given ADCP.
2. This friction map is used in the model to produce a velocity time series at a different, desired time period. This can then be used for calibration, whilst only the original data is used for validation.

For example, at the final stage of the data assimilation experiment described in Section 2.4, the 2013 and 2017 data will have been projected to the 2022 time period to be used alongside the latest measured data. This technique is discussed in Section 5.3.

### 3.4. Performance Metrics

Whilst the objective function of the adjoint-based optimisation is formulated using the root mean squared error of the velocity magnitudes of the ADCP, other metrics are often used to indicate model performance. We split the ADCP accuracy into velocity magnitude (i.e., speed) and direction.

#### 3.4.1. Speed Rating

The speed rating is calculated based on the coefficient of determination $\left(R^2\right)$ of the velocity magnitude distribution (i.e., values sorted into ascending order) and the normalized root mean square error (NRMSE) of the signal. These values are calculated for each individual flood and ebb cycle, and averaged over the entire simulation period for each tidal direction. The rating is computed as:

$$\mathcal{R}_{\text{speed}} = 100\left(0.5 \times \overline{R^2_{\text{tide}}} + 0.5 \times \left(1 - \overline{\text{NRMSE}_{\text{tide}}}\right)\right),$$

where $\overline{R^2_{\text{tide}}}$ is the average $R^2$ value calculated for each tidal cycle, and $\overline{\text{NRMSE}_{\text{tide}}}$ is the average NRMSE over all tidal cycles.

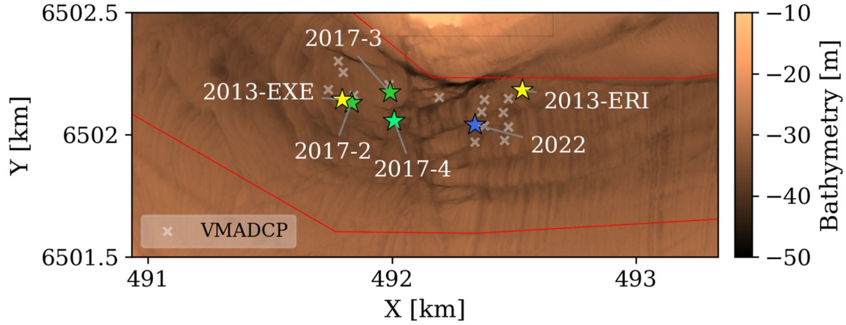


**Figure 2.** ADCP locations overlaid on high resolution bathymetry surveyed for the MeyGen project. Crosses indicate vessel mounted (VM) ADCPs used to retrospectively correct measured principal directions. Projection: UTM Zone 30N.

It is important to note that using the sorted values for $R^2$ for the whole simulation period (typically $\approx$ 1 month) could lead to misleading error statistics, as this disregards the phase of the velocity signal altogether. By determining these values for each individual cycle and then averaging them, the fit incorporates how well the variation between cycles is modeled. On the other hand, the phase of the velocity signal does not change the total kinetic energy expected over a time period at a given point, thus the incorporation of $R^2$ in addition to NRMSE, to reduce the role that phase plays in determining the rating metric.

Based on the above combination, a rating of 100 infers perfect emulation of the measured velocity magnitude data.

#### 3.4.2. Direction Rating

Principal flow directions at ADCP stations remain mostly uniform (with the exception of some eddying features) within the duration of their data collection period. Variation around the mean exists due to turbulence, but the range also remains consistent. Thus, rather than generating a rating for the direction, we simply present the angular difference in the principal tidal directions.

#### 3.4.3. Elevation

We present the key harmonic amplitudes and phases (M2 and S2) at nearby tide gauges to indicate the sensitivity of the modeled elevations to velocity data assimilation. These data are not assimilated and therefore provide a validation of the large-scale barotropic response of the model.

Given that the adjoint optimisation targets spatially localized bottom friction, we do not expect substantial modification of basin-scale tidal elevations. Instead, this analysis is intended to verify that the optimisation preserves the correct tidal propagation characteristics.

## 4. Results

### 4.1. Calibration Signal Duration Sensitivity

Calibration was initially performed on the 2013 data over a maximum of 50 iterations (or until optimisation convergence) to indicate the minimum number of optimisation iterations to be used in the study. The cost function gradient evolution in Figure 3 indicates that 35 iterations appeared sufficient, beyond which, minimal further gains were made. This exercise was conducted for different calibration time periods, whereby the respective cost function trends indicate that the optimisation process is generally converging.

Table 3 presents the sensitivity of the calibrated solution to the number of flood and ebb cycles included in the calibration. As anticipated, increasing the number of cycles used in the calibration increases confidence to the model's predictive capability. However, the benefit beyond 3 cycles tails off, relative to the added computational cost for the calibration process. Therefore, 3 flood/ebb cycles were used for the remainder of the study. A second observation from Table 3 is the variation in performance at different stations. ADCP 2017-4 shows an example where increasing the number of cycles used generally increases performance in both the flood and ebb

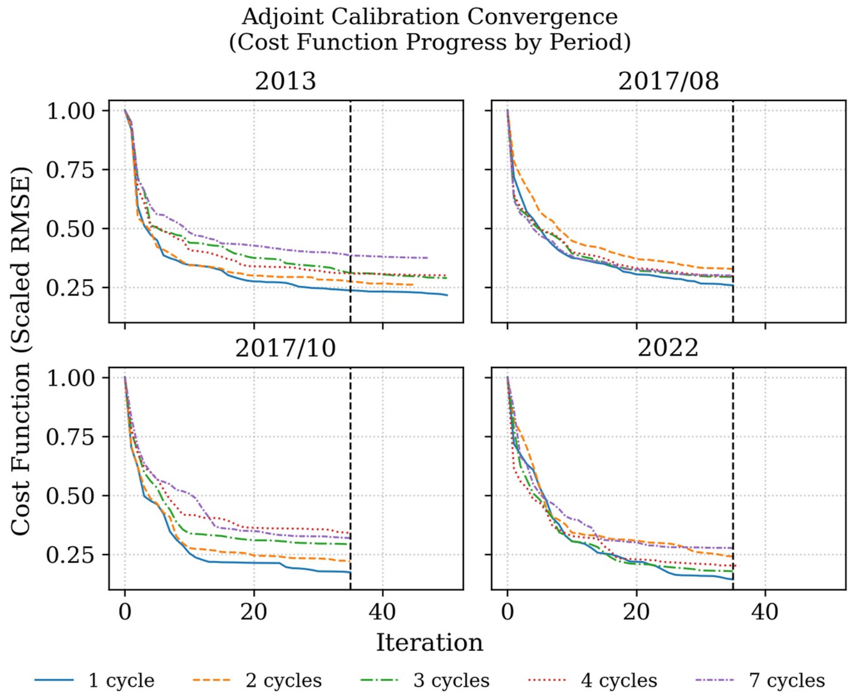


**Figure 3.** Convergence of loss function using different time periods and cycle durations for the calibration procedure. The cost function (scaled RMSE) is for training only and scaled for comparison to demonstrate convergence.

simultaneously. ADCPs 2017-2 and 2017-3 on the other hand, show increasing flood performance as the number of cycles improves, whilst the ebb performance varies.

### 4.2. Benchmark Cases

Tables 4–7 summarize the performance metrics of the difference cases of the calibration exercise. The best performing uniform value of Manning coefficient was $n_M = 0.04$ s m$^{-1/3}$ (other uniform results omitted for brevity). In terms of velocity magnitude, this case performs well for the 2013 data as shown in Figure 4, with the exception of 2013-ERI flood tides. With a uniform global value, altering the resistance could lead to improved

**Table 4**
*Calibration Speed Rating Deviation From Uniform Benchmark Metrics for Different Calibration Cases for* ***Ebb*** *Tides*

| | ADCP | | | | | | | | | | |
|---|---|---|---|---|---|---|---|---|---|---|---|
| | Inner Sound | | | | | | | Outer Sound | | | |
| | 2013 | | 2017 | | | | | 2001 | | | |
| Calibration case | ERI | EXE | 2 | 3 | 4 | 2022 | Average | C1 | C2 | C3 | Average |
| Uniform | 93.3 | 93.6 | 94.3 | 92.8 | 90.3 | 92.0 | **92.7** | 73.6 | 90.3 | 89.7 | **84.5** |
| Sedimentological | −1.4 | −0.8 | −1.0 | +1.5 | 0.0 | −0.7 | **−0.4** | −5.6 | −4.1 | +0.1 | **−3.2** |
| 2001 | −1.0 | −1.0 | +0.8 | −2.0 | −1.0 | −0.6 | **−0.8** | +15.3 | +1.7 | +1.7 | **+6.2** |
| 2013 | +0.7 | +0.4 | +0.7 | +2.0 | +0.2 | −0.3 | **+0.6** | +8.9 | +0.3 | +0.2 | **+3.1** |
| 2013/17a | +0.5 | +0.2 | +0.7 | +0.2 | −0.2 | +0.8 | **+0.4** | +9.9 | −0.2 | +0.6 | **+3.4** |
| 2013/17b | +0.7 | +0.2 | +0.4 | −0.3 | +0.5 | +1.2 | **+0.5** | +9.1 | +0.7 | +0.2 | **+3.3** |
| 2013/17/22 | +0.7 | +0.4 | +0.6 | +0.4 | +0.4 | +0.3 | **+0.5** | +12.5 | −0.1 | +0.6 | **+4.3** |
| All | +1.0 | +0.4 | −0.1 | +0.3 | +0.2 | −0.2 | **+0.3** | +16.2 | +2.2 | +1.2 | **+6.5** |

*Note.* The rating, out of 100, is a combination of cycle-wise $R^2$ and NRMSE metrics as described in Section 3.4.

**Table 5**
*Calibration Speed Rating Deviation From Uniform Benchmark Metrics for Different Calibration Cases for **Flood** Tides*

| | ADCP | | | | | | | | | | |
|---|---|---|---|---|---|---|---|---|---|---|---|
| | Inner Sound | | | | | | | Outer Sound | | | |
| | 2013 | | 2017 | | | | | 2001 | | | |
| Calibration case | ERI | EXE | 2 | 3 | 4 | 2022 | Average | C1 | C2 | C3 | Average |
| Uniform | 89.5 | 93.0 | 94.3 | 94.6 | 90.1 | 91.0 | **92.1** | 86.0 | 90.8 | 83.9 | **86.9** |
| Sedimentological | +0.8 | −0.7 | −0.3 | −1.7 | −1.2 | −1.9 | **−0.8** | −9.9 | −2.3 | −2.9 | **−5.0** |
| 2001 | +3.4 | +0.9 | +0.9 | +1.8 | +1.4 | +2.2 | **+1.8** | +2.7 | +1.9 | +5.8 | **+3.5** |
| 2013 | +3.5 | +1.3 | +2.1 | −0.8 | +1.4 | +0.8 | **+1.4** | +3.4 | +0.8 | +3.5 | **+2.6** |
| 2013/17a | +2.5 | +1.0 | +2.1 | +1.2 | +1.1 | +1.9 | **+1.6** | +2.4 | +0.7 | +3.3 | **+2.1** |
| 2013/17b | +2.5 | +1.2 | +2.0 | +0.9 | +1.5 | +2.0 | **+1.7** | +2.3 | +0.5 | +4.2 | **+2.3** |
| 2013/17/22 | +2.8 | +1.1 | +2.0 | +1.2 | +1.3 | +1.6 | **+1.7** | +2.8 | +1.4 | +3.4 | **+2.5** |
| All | +3.2 | +1.5 | +2.1 | +1.3 | +1.6 | +1.9 | **+1.9** | +3.9 | +1.9 | +5.1 | **+3.6** |

*Note.* The rating, out of 100, is a combination of cycle-wise $R^2$ and NRMSE metrics as described in Section 3.4.

flood tide performance, but would sacrifice ebb tide performance leading to over-estimations. Tables 4 and 5 quantify the performance numerically for the speed rating.

For direction, performance for the 2013 data is similar to the magnitude, with reasonable agreement (within 1.5°) in principal direction except for the ERI flood tide. However, the performance against 2017 data during the ebb tide, is particularly reduced, with discrepancy between the two above 3°.

The best results for a sedimentological approach result from using the maximum values of particle diameter for Equation 9. The resultant friction map is shown in Figure D2 and varies across the domain but is predominantly uniform within the Inner Sound itself. Relative to the uniform friction coefficient assumption, the sedimentological mapping performance is poorer in terms of velocity magnitude overall, faring better only at select stations over certain tides. Both show poorer performance on the flood than the ebb for magnitude. Directional discrepancy is slightly reduced using the sedimentological mapping approach in ebb tides but increases in flood tides, indicating that a uniform friction coefficient approach is superior for the mesh and viscosity used in this case. The uniform friction case sees an equal level of average discrepancy whilst the sedimentological distribution of friction has greater discrepancy in predicting the flood principal direction across stations.

**Table 6**
*Calibration Direction Discrepancy (°) for Different Calibration Cases for **Ebb** Tides*

| | ADCP | | | | | | | | | | | | |
|---|---|---|---|---|---|---|---|---|---|---|---|---|---|
| | Inner Sound | | | | | | | | Outer Sound | | | | |
| | 2013 | | 2017 | | | | | | 2001 | | | | |
| Calibration case | ERI | EXE | 2 | 3 | 4 | 2022 | Average | Std Dev. | C1 | C2 | C3 | Average | Std Dev. |
| Uniform | 1.4 | 1.2 | 3.4 | 2.7 | 3.0 | 0.8 | **2.1** | 1.0 | 6.2 | 0.2 | **7.9** | **4.8** | **3.3** |
| Sedimentological | 0.8 | 1.1 | 3.5 | 2.3 | 2.9 | 0.7 | **1.9** | 1.1 | 4.1 | 0.8 | **5.0** | **3.3** | **1.8** |
| 2001 | 0.9 | 1.9 | 4.4 | 3.5 | 3.7 | 0.9 | **2.5** | 1.4 | 1.1 | 0.9 | **4.9** | **2.3** | **1.8** |
| 2013 | 0.6 | 0.0 | 2.8 | 1.6 | 1.7 | 0.4 | **1.2** | 0.9 | 6.1 | 0.5 | **8.3** | **5.0** | **3.3** |
| 2013/17a | 0.7 | 0.9 | 1.0 | 0.2 | 0.2 | 0.8 | **0.6** | 0.3 | 6.1 | 0.9 | **7.9** | **5.0** | **3.0** |
| 2013/17b | 0.9 | 0.1 | 1.8 | 0.7 | 0.5 | 1.5 | **0.9** | 0.6 | 6.1 | 0.1 | **8.1** | **4.8** | **3.4** |
| 2013/17/22 | 0.3 | 0.6 | 1.2 | 0.1 | 0.2 | 0.0 | **0.4** | 0.4 | 5.1 | 0.3 | **7.9** | **4.4** | **3.1** |
| All | 0.1 | 0.2 | 2.0 | 0.6 | 0.5 | 0.4 | **0.6** | 0.6 | 4.1 | 0.4 | **5.0** | **3.2** | **2.0** |

**Table 7**
*Calibration Direction Discrepancy (°) for Different Calibration Cases for **Flood** Tides*

| | ADCP | | | | | | | | | | | | |
|---|---|---|---|---|---|---|---|---|---|---|---|---|---|
| | Inner Sound | | | | | | | | Outer Sound | | | | |
| | 2013 | | 2017 | | | | | | 2001 | | | | |
| Calibration case | ERI | EXE | 2 | 3 | 4 | 2022 | Average | Std Dev. | C1 | C2 | C3 | Average | Std Dev. |
| Uniform | 3.5 | 0.7 | 1.8 | 2.9 | 1.8 | 1.9 | **2.1** | 0.9 | 1.5 | 5.2 | **2.2** | **3.0** | **1.6** |
| Sedimentological | 5.3 | 1.2 | 2.3 | 2.9 | 2.4 | 3.3 | **2.9** | 1.3 | 0.6 | 0.6 | **3.1** | **1.4** | **1.2** |
| 2001 | 0.4 | 0.7 | 1.6 | 2.4 | 1.2 | 0.8 | **1.2** | 0.7 | 0.3 | 2.6 | **6.6** | **3.2** | **2.6** |
| 2013 | 0.2 | 0.5 | 1.1 | 1.7 | 0.2 | 0.7 | **0.7** | 0.5 | 1.4 | 5.5 | **9.7** | **5.5** | **3.4** |
| 2013/17a | 0.2 | 0.5 | 0.3 | 0.7 | 2.1 | 1.4 | **0.9** | 0.7 | 1.4 | 4.8 | **9.1** | **5.1** | **3.2** |
| 2013/17b | 0.4 | 0.7 | 0.6 | 0.2 | 1.3 | 1.5 | **0.8** | 0.5 | 1.4 | 5.2 | **3.9** | **3.5** | **1.6** |
| 2013/17/22 | 1.2 | 0.5 | 0.5 | 0.3 | 1.7 | 0.5 | **0.8** | 0.5 | 1.2 | 5.5 | **10.1** | **5.6** | **3.6** |
| All | 0.8 | 0.5 | 0.2 | 0.3 | 1.3 | 0.8 | **0.7** | 0.4 | 0.5 | 2.1 | **7.2** | **3.3** | **2.9** |

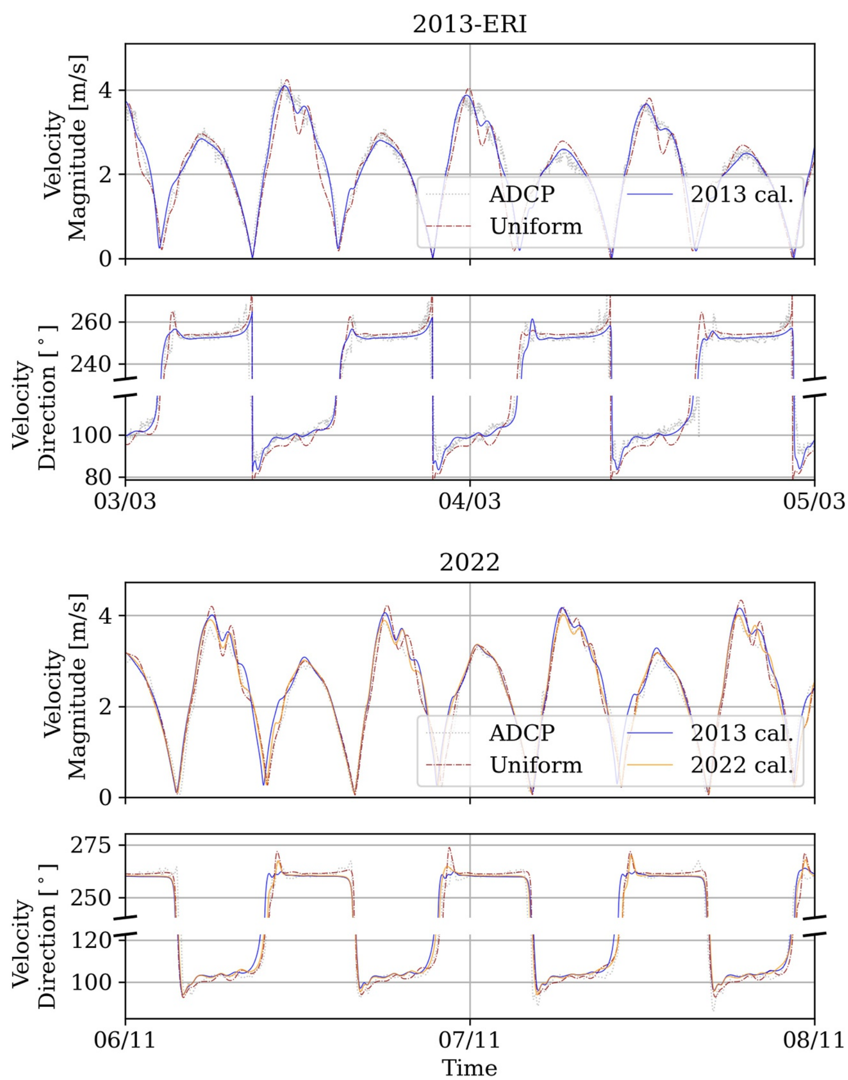


**Figure 4.** Comparison of ADCP data to modeled velocities for different calibration cases over different validation periods.

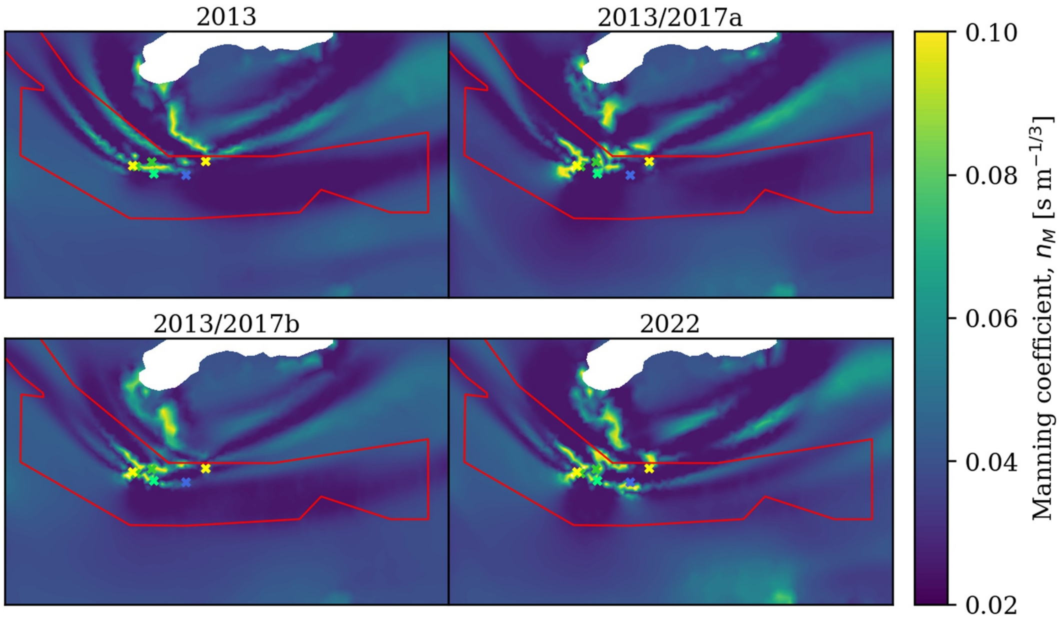


**Figure 5.** Final Manning's $n_M$ coefficient fields from adjoint calibration for varying levels of data provision. The ADCP locations are scattered on for reference. Projection: UTM Zone 30N.

### 4.3. Adjoint-Based Calibration

Figure 5 shows the $n_M$ friction coefficient fields for each adjoint-based calibration case. As more stations are added to the optimisation, we see more sharp localized changes introduced to reproduce velocity signals across stations.

Relative to the uniform friction coefficient case, the initial calibration for the 2013 data improves on the ERI ADCP's flood magnitude, whilst maintaining good performance in the flood and ebb at the EXE ADCP location. Critically, the directional discrepancy is reduced from 3.5 to 0.2° for the ERI station during the flood, whilst also further improving the already good agreement in the ebb. In the absence of the 2017 data, magnitude performance remains strong relative to other cases on Stations 2 and 4 for both ebb and flood tides. For 2017-3 flood magnitude, and for nearly all 2017 directions, performance drops notably. The ebb magnitude performance is prioritized over the flood, as indicated by the later calibration runs. Conversely, flood directions aside from the 2017 stations are in good agreement, with poorer performance in the ebb.

Assimilation of the 2017-08 data leads to significant improvement in directional agreement, with a change in bias toward the flood in magnitude performance. Including the 2017-4 station leads to little improvement beyond reducing the discrepancy in principal directions at that station. Finally, introduction of the 2022 data leads to the most uniform improvement in magnitude performance, with every single station in each tidal direction improving relative to the baseline. Overall, the majority of improvement is found in the flood tides, as they are associated with higher velocities.

Figure 6 shows the subtle improvement in principal direction once the model is calibrated. Prior to calibration, the model predictions uniformly misalign against measured data, with ebb directions toward the west of the site predicted to be further north. Whilst these initial directional discrepancies seem small in the context of general ocean modeling, they would propagate downstream in any array design decision-making where wake interactions become critical.

### 4.4. Implications on Current Energetics

Resource availability maps for a semi-idealized 3MW device are shown in Figure 7, as mean extractable power over a representative duration. This is calculated based on the duration of the 2022 ADCP deployment, rather than an entire a year and serves to demonstrate the impact of spatially varying calibration on potential resource. The relative difference in extractable power across cases suggests the adjoint-based calibration leads to a reduction in

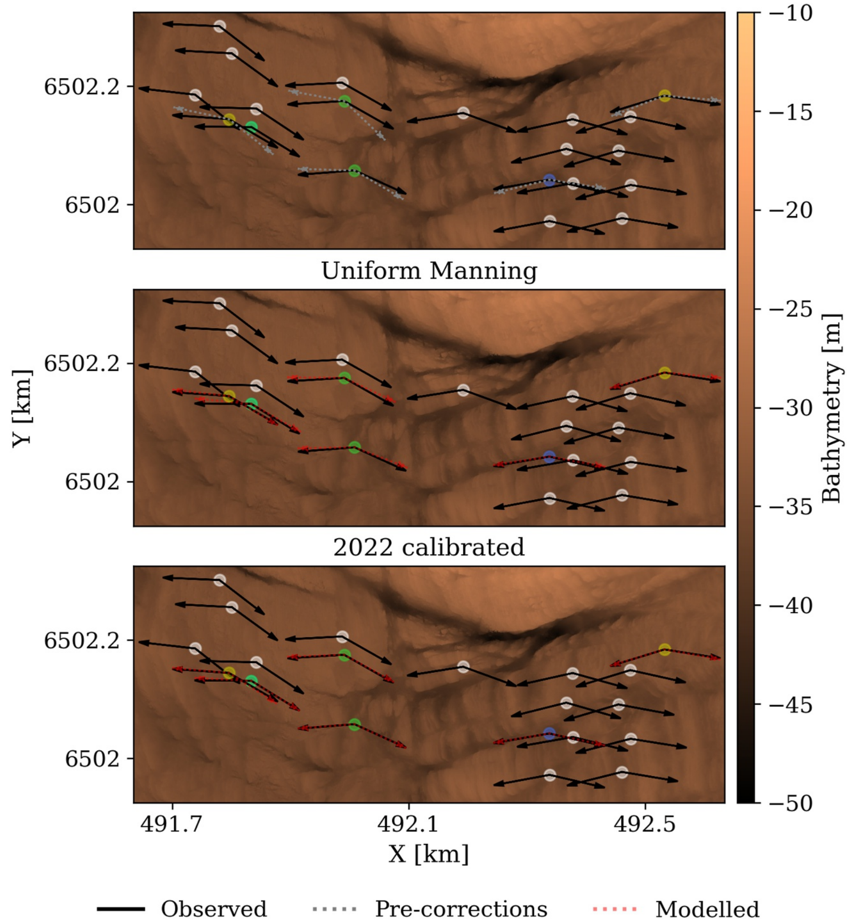


**Figure 6.** Principal directions for different models compared to corrected measured data, overlaid on high resolution bathymetry surveyed for the MeyGen project. White dots indicate vessel mounted ADCP measurements used to correct the seabed principal directions, as shown in the top inset. Seabed mounted ADCPs are labeled in Figure 2. Projection: UTM Zone 30N.

potential energy yield predicted in the west of the site, with an increase across the majority of the rest of the site. Just north east of the lease area, there is substantial reduction in the potential resource. There, a sand dune is present (Figure D2) and hence could coincide with the calibration correcting the model for its under-resolved effects. Similarly, there are notable changes of friction and this is mirrored to the resource map near the south west tip of Stroma, changing the global shear flow profile at the lee of the island. This could be indicative of potential errors in the geography or bathymetry data at the coastline that inform the model.

We next consider the effect of assimilation on the flow and energy flux through the channel. Tables 8 and 9 summarize volumetric flow rate changes and kinetic energy fluxes through transects (see Figure 1) in the Inner and Outer Sound on a case-by-case basis. Applying the sedimentological Manning coefficient mapping approach leads to increased flow and energy through the entire domain, as the friction throughout is much lower and the boundaries are only forced by tidal elevation. In contrast, calibration to the Outer Sound data only (2001) leads to reduced flow and kinetic energy fluxes through the channel due to an increase in channel friction, with an accompanying increase to the flow and energy fluxes for the Inner Sound.

Conversely, for calibration that includes data from the Inner Sound, the flow and fluxes in the Outer Sound continuously drop as more stations are introduced. We observe that as each station is added, more friction is also introduced to the model. It appears the increased friction in the overall Pentland Firth causes changes to the full channel (i.e., outer and inner channel) dynamics, rather than at the constrained sub-channel scale. Likewise, within the Inner Sound itself, the average flow rate and inlet kinetic energy flux generally drops as more friction is added to modify the local flow. With the exception of the 2013 case, where only 2 ADCPs have been included, the flow rate

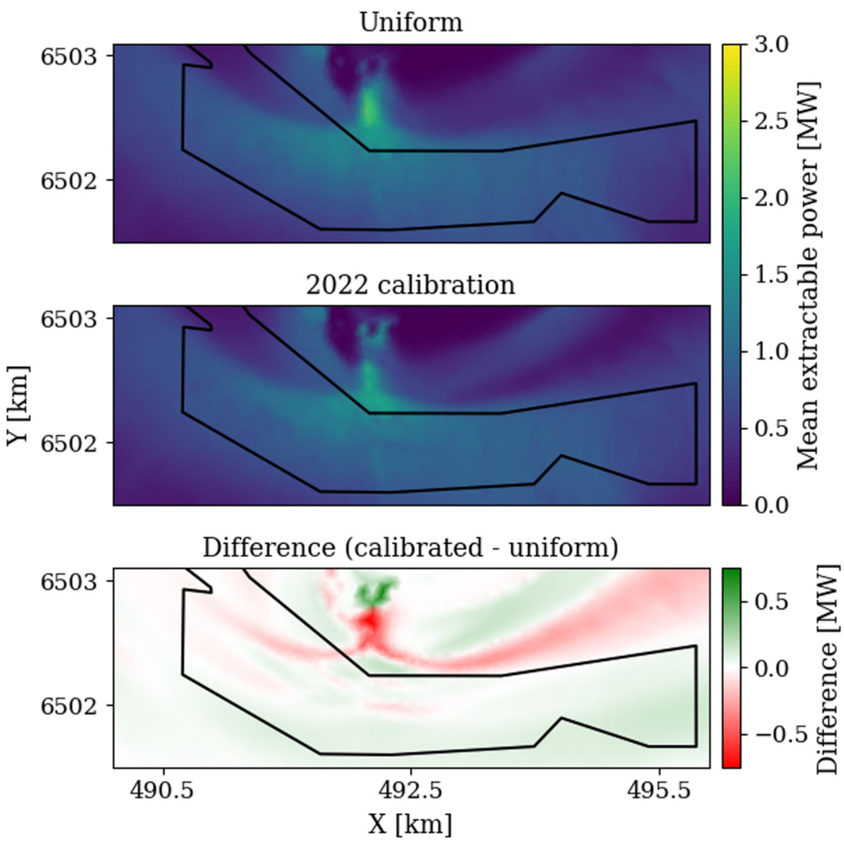


**Figure 7.** Resource maps based on a 3MW device for the uniform versus calibrated cases. Potential resource assessed at each location over the 2022 ADCP validation period. Rotor-averaged velocities are determined using average measured velocity profiles. Black outline indicates MeyGen lease area. Projection: UTM Zone 30N.

is always reduced relative to the benchmark uniform case. However, the kinetic energy flux may still increase relative to the baseline. Due to the dependency on the cube of the velocity, an overall increase in friction may still lead to increased kinetic energy through certain transects as flow accelerates as by-pass flow around patches of increased frictional resistance. At the inlet, except the first few cases, the kinetic energy flux decreases. By the centre of the Inner Sound, the kinetic energy flux tends to be higher, whilst at the outlet, it increases more substantially.

**Table 8**
*Average Volumetric Flow Rates in ADCP 2022 Time Period Relative to the Uniform Benchmark Case*

| | (Change in) volumetric flow rate $(\mathrm{m}^3\ \mathrm{s}^{-1})$ | | | |
|---|---|---|---|---|
| | Flood | | Ebb | |
| Calibration case | Inner Sound | Outer Sound | Inner Sound | Outer Sound |
| Uniform | 90,540 | 587,733 | 78,740 | 636,108 |
| Sedimentological | +5.67% | +4.04% | +0.80% | +4.48% |
| 2001 | +1.98% | −1.64% | +2.10% | −2.63% |
| 2013 | +1.48% | −0.47% | +0.72% | −1.13% |
| 2013/17a | −0.28% | −0.87% | −0.73% | −1.40% |
| 2013/17b | −0.36% | −0.84% | −0.42% | −1.94% |
| 2013/17/22 | −0.99% | −1.57% | −1.51% | −1.00% |
| All | −1.39% | −2.16% | −0.60% | −1.94% |

### 4.5. Elevation Agreement

Table 10 summarizes the amplitudes and phases for the M2 and S2 constituents at the closest tide gauges. As the adjoint calibration led to little change beyond the Inner Sound, the results do not vary significantly between uniform and adjoint-calibrated cases. Across all cases and including the sediment-based approach, amplitude differences remain within $\mathcal{O}(0.01\ \mathrm{m})$ and phase differences within 1.5°, indicating that the calibration preserves the large-scale tidal dynamics of the system.

The limited sensitivity of tidal elevations to the optimisation reflects the spatial scale of the control variable. The adjoint modifies bottom friction in highly localized regions (see Figure D2), whereas tidal elevations at Wick and Scrabster are governed by basin-scale pressure gradients and boundary forcing. As a result, localized changes in dissipation primarily redistribute velocity and energy flux within channels without significantly altering the external tidal signal. This behavior is consistent with the changes observed in volumetric

**Table 9**
*Average Kinetic Energy Fluxes in ADCP 2022 Time Period Relative to the Uniform Benchmark Case*

| | (Change in) kinetic energy flux (MW) | | | | | | | |
|---|---|---|---|---|---|---|---|---|
| | Flood | | | | Ebb | | | |
| | Inner Sound | | | | Inner Sound | | | |
| Calibration case | Inlet | Centre | Outlet | Outer Sound | Inlet | Centre | Outlet | Outer Sound |
| Uniform | 141.04 | 264.95 | 299.23 | 2223.12 | 183.88 | 180.91 | 121.04 | 2528.70 |
| Sedimentological | +11.2% | +13.4% | +11.0% | +17.6% | +5.0% | +6.9% | +4.5% | +16.6% |
| 2001 | −0.5% | +0.4% | +16.4% | −4.2% | −0.7% | +6.7% | +6.8% | −8.5% |
| 2013 | +5.9% | +8.9% | +24.8% | −2.4% | +3.6% | +6.0% | +7.4% | −4.2% |
| 2013/17a | +1.4% | +5.3% | +21.4% | −2.1% | +4.4% | +3.7% | +3.8% | −3.9% |
| 2013/17b | −2.3% | +2.3% | +21.2% | −3.5% | +2.0% | +5.1% | +1.8% | −5.6% |
| 2013/17/22 | −0.7% | +0.6% | +12.6% | −4.4% | −3.0% | +2.1% | −0.7% | −4.5% |
| All | −4.4% | −3.1% | +10.3% | −6.7% | −1.8% | +2.7% | +1.2% | −7.8% |

flow (Table 8), whereby substantial changes (Figure D2) to the bottom friction must be made to impact the flux, which is most sensitive to tidal boundary forcing.

## 5. Discussion

### 5.1. Model Sensitivity

The combination of viscosity and bed friction influence mixing and current flow. The larger the value of the eddy viscosity, the more rapidly turbulent structures are dispersed. The greater the value of the bed friction, the more energy is dissipated as the current flows over the seabed. An appropriate value for either, but particularly the viscosity, is dependent on the domain size and mesh resolution. Initial sensitivity studies (not shown) found that small perturbations to a low friction coefficient ($n_M = 0.02$ s m$^{-1/3}$) model with "low" viscosity (1 m$^2$ s$^{-1}$) lead to drastic changes in model output. With high friction coefficient values (e.g., $n_M = 0.05$ s m$^{-1/3}$) and higher eddy viscosity (5 m$^2$s$^{-1}$), this behavior does not occur and factors such as spin-up duration, simulation start time and model timestep do not alter the convergence to the same model velocity state shortly after the model run has started. The former observation is in agreement with Warder and Piggott (2022), where it was also found that a model of lower friction may perform better with a higher viscosity value and ideally these would be simultaneously optimized. Our initial sensitivity studies are also in agreement that model sensitivity is dampened by higher viscosity, such that small perturbations will not lead to large changes in predicted model states. Adjoint-based calibration reacts sensitively to an unstable model, so we elected to use a higher viscosity value of 5 m$^2$ s$^{-1}$, with a lower limit of 0.025 s m$^{-1/3}$ applied for the Manning coefficient. It should be noted that the eddy viscosity itself can be spatially varying (e.g., via turbulence modeling), with respective implications downstream on how the energy extraction is modeled. For simplicity, a uniform viscosity was imposed for this study.

**Table 10**
*Amplitude and Phase Discrepancies at Wick and Scrabster Gauges*

| | Amplitude (m) | | | | Phase (°) | | | |
|---|---|---|---|---|---|---|---|---|
| | Wick | | Scrabster | | Wick | | Scrabster | |
| Station | M2 | S2 | M2 | S2 | M2 | S2 | M2 | S2 |
| Measured | 1.02 | 0.35 | 1.35 | 0.49 | 322.3 | 0.3 | 243 | 276 |
| Uniform | 0 | +0.02 | −0.03 | +0.02 | −1.5 | −0.5 | −0.7 | +1.2 |
| Sedimentological | 0 | +0.02 | 0.00 | +0.04 | +0.2 | +1.2 | −0.5 | +1.2 |
| 2001 | 0 | +0.02 | −0.03 | +0.03 | −1.2 | −0.3 | −0.8 | +1.3 |
| 2013 | 0 | +0.02 | −0.03 | +0.02 | −1.4 | −0.5 | −0.7 | +1.1 |
| 2013/17a | 0 | +0.02 | −0.02 | +0.03 | −1.4 | −0.5 | −0.7 | +1.1 |
| 2013/17b | 0 | +0.02 | −0.03 | +0.03 | −1.4 | −0.5 | −0.7 | +1.1 |
| 2013/17/22 | 0 | +0.02 | −0.02 | +0.03 | −1.4 | −0.4 | −0.8 | +1.1 |
| All | 0 | +0.02 | −0.03 | +0.03 | −1.2 | +0.5 | −0.9 | +1.3 |

*Note.* Modeled values are averaged over each validation period. Negative Δ values indicate counter-clockwise phase discrepancy.

### 5.2. Bottom Friction Distribution

#### 5.2.1. Benchmark Cases

The best-performing uniform friction coefficient (i.e., $n_M = 0.04$) leads to good agreement with several ADCP deployments. However, agreement against some ADCPs could be deemed satisfactory in only one (i.e., flood/ebb) tide. Improving performance for the opposite tide by further tuning corresponds to a trade-off in performance relative to the initially well performing tide. Similarly, it was found that the best uniform friction coefficient performed particularly well for the majority of the 2013 data, but less so for the 2017 data, particularly in terms of velocity direction. Therefore, at this site, determining a spatially varying bottom friction distribution is necessary to accurately capture the spatio-temporal variation in velocity.

Use of a sedimentological based mapping of the friction coefficient led to no overall improvement against measured data. To maintain meaningful physical values, a Bayesian inference approach could be deployed, such as that demonstrated for the Bristol Channel by Warder et al. (2022). This also has the benefit of providing a probability distribution, inferring the uncertainty in the bottom friction parameter for each sediment type. However, there are numerous issues with this approach. Firstly, the description of a sediment in one area may match another, but this does not necessarily correspond to the same value of bottom friction. Thus, each region needs to be individually tuned, increasing the number of optimisation parameters. Furthermore, the regions themselves are very loosely defined based on limited recordings of sediment type. Therefore, there is significant uncertainty in the region definition, and this could form its own optimisation problem. As optimisation control variables increase, this then points back toward an adjoint-based approach where friction is allowed to vary more freely across the computational domain.

### 5.2.2. Adjoint-Based Outputs

The adjoint-based calibration with no regularization lead to sharply changing distributions of Manning coefficient. This is consistent with the findings of (Kärnä et al., 2023). However, considering the small distances between ADCPs, more localized changes are required to modify the flow. We found that using a Hessian based regularization reduced the agreement against measured predictions (Appendix D). It smoothens the non-regularized field by design, which is ineffective when measurements are in such close proximity and mesh resolution is relatively large to ADCP separation. An independent points scheme approach showed more promise and further investigation is required to determine the optimal method for regularization, in combination with increasing mesh resolution. With any form of regularization, the distribution of Manning coefficient was sensitive to the number of ADCPs used and as more were added, performance generally increased.

Regardless of the approach to spatially regularizing the bottom friction, it represents tuning the model for physics that are not adequately represented. The representative roughness should account not only for skin and form friction, but also for subgrid roughness scales (Ouda & Toorman, 2019). Mesh resolution will play an important role in the accuracy of the model generally, but also impact the optimal tuning of the bottom friction. In previous iterations of the model with finer mesh resolution, the sedimentological approach has provided better agreement than a uniform friction. With smaller elements, the model can capture higher-frequency variations and less artificial spreading of diffusive behavior (Banerjee et al., 2024). Thus, the optimal bottom friction distribution, whether Manning, Chezy, quadratic etc., is also mesh- and model-dependent. We note however, that engineering models need to be robust and computationally efficient for the problem they are representing. Thus, a model for array design will likely be a well-tuned 2D depth-averaged SWE model, with an understanding of its limitations. When greater fidelity is required, more accurate representation of the physics is introduced at greater cost, likely with further tuning requirements.

## 5.3. Calibration Data

Where the purpose of modeling is resource assessment and array design, calibration to velocity is required, rather than elevation alone. ADCPs are typically used, particularly in investigating turbulence. However, most studies use a very limited number of velocity validation points, largely due to cost and complexity of further deployments. As discussed in Section 5.2, this can cause misleading results or over-fitting. Another consequence of limited data, is reduced confidence in the data itself. Figure 6 shows the principal directions of the raw data pre- and post- an additional vessel mounted ADCP survey. With the additional vessel mounted data, it becomes clear that there have been compass calibration or frame movement issues, particularly in ADCP2017-3, for example. The seabed mounted data typically has uncertainty in the measured direction of <5°, if compass calibration has been adequately calibrated and the correct device has been used. It is known in this case for example, that both 2013 and the 2022 ADCP had frame movement issues which should not affect the magnitude reading but did require corrections for the direction. Thus, more devices help reduce uncertainty in the overall flow behavior of the site, and vessel mounted campaigns can assist improving the quality of more expensive seabed mounted deployments. In Figure 6, the vessel mounted data is assumed to be correct in direction, but in reality it is subject to uncertainty and could have its own compass calibration issues. To determine the resource magnitude and investigate turbulence, direction has been sub-critical, but as array design requires constraining wake interactions, more effort is required to ensure that the flow direction is accurately captured.

Another challenge is the number of devices that can simultaneously be deployed. Particularly given the financing mechanisms for array developers, it is often the case that measurement campaigns also become staggered. Figure 6 shows the principal directions of ADCPs from four different time periods. At these locations, the seabed is relatively bare of sediments and thus geomorphological changes are unlikely, allowing such comparison with reasonable confidence. Nonetheless, it becomes challenging to calibrate a model as the signal needs to either be extrapolated or the model must be calibrated over multiple time periods. When enumerating through uniform or sedimentological-based bottom friction maps, this requires a linearly increasing time for each period of available data. Likewise, when using a gradient-based approach to tune the model, this not only requires increasing the time for each calibration as another forward run is added, but also increased memory requirements. To remain within the constraints of the computational unit, this requires shortening the duration of the calibration period. This leads to a potential temporal over-fitting. The alternative of extrapolating data is challenging but allows reduced time and memory consumption. Harmonic analysis is ineffective due to non-deterministic effects (Warder et al., 2021), but can be used as a basis for machine learning techniques as displayed in Monahan et al. (2023). Here, we use the model calibration runs to extrapolate the velocity signals, providing an alternative physical basis. This can be done with an intentionally spatially over-fit model to maximize the accuracy with respect to a single location. Regardless of the extrapolation method, uncertainty will exist, though likely within a similar scale to the uncertainty of the measured readings.

Six stations were used within the Inner Sound, and with each station added, performance was improved overall, particularly with respect to direction. However, the distribution of bottom friction remains notably sharp. Appendix D shows the results of introducing spatial regularization. However, 6 ADCPs deployed at different times is still a limited number across such a spatially complex site. In this study, it leaves no additional points in space to compare to. The importance of compass calibration and the need for alternative methods of data collection is clear for improved spatial coverage of the site at a reduced cost. In that regard, future work could include calibrating to the vessel mounted survey data and validating against the seabed mounted data.

### 5.4. Flow Redistribution Under Spatially Varying Friction

The adjoint-based calibration modifies the spatial distribution of bottom friction, leading to changes in velocity structure and energy fluxes throughout the domain. Tables 8 and 9 indicate whilst the velocity agreement may have improved when data from both the Inner and Outer Sound was included, there were changes to the modeled fluxes due to spatial redistribution of the bottom friction. However, as demonstrated in Section 4.5, these modifications do not significantly alter the large-scale tidal elevations. Within the Inner and Outer Sound, the most notable deviations existed between the baseline cases, as the sedimentological approach introduces significant variation in Manning's $n_M$ away from the Pentland Firth. Instead, the primary effect of the optimisation is the redistribution of flow within and between channels rather than extensive modification of the entire domain.

Calibration of channel scale dynamics is challenging in the absence of additional ADCPs at inlets and outlets to various channels within the domain, or without imposing the volumetric flow rate at the boundaries. Forcing with only the elevation means the need for multiple ADCPs and tide gauges to ensure correct volumetric flows throughout the domain, whilst relying on interpolated tidal forcing data of low spatial resolution for volumetric forcing is also fraught with uncertainty. With ADCPs limited to a single or couple of channels, and the initial friction mapping based only on the channel of interest, it is unlikely that the model is accurate in other locations. This is demonstrated by the poor cross-channel performance of models calibrated exclusively to either Inner or Outer Sound observations.

In addition to increasing the spatial coverage of ADCP measurements, elevation data remain important for constraining basin-scale dynamics. The present results show that localized calibration of bottom friction has little impact on tidal elevations at distant gauges. Greater sensitivity would be expected from changes acting over larger spatial scales, or at key locations that influence the overall impedance of the system. In practice, tidal elevations are also strongly controlled by the prescribed boundary forcing, which will have a larger influence than local friction adjustments within individual channels, unless open water boundaries are substantially extended relative to the region of interest. Given that tidal forcing atlases are typically global and relatively low resolution, there is likely scope for improving boundary conditions alongside friction calibration as more data become available

(Thiébot et al., 2026). Combining distributed velocity measurements with independent elevation observations is therefore important for constraining both local flow structure and larger-scale tidal behavior. Future work will consider how regional friction and boundary forcing can be adjusted together to better represent both velocity and elevation fields.

### 5.5. Implications for Tidal Turbine Array Development

Given the financing mechanisms for array developers in the UK, emphasis on obtaining calibration and validation data is critical for future sites. Figure 7 demonstrates the change in assumed resource availability with changes in the model due to calibration data availability. The margins of array developers are currently slim and the levelised cost of energy far larger than alternative forms of more established renewable energy. Presenting accurate model concordance is therefore critical in obtaining funding from investors. An overestimate in initial resource will lead to the developer needing to find alternative methods to increase profitability. One of the key methods to do this is array optimisation to provide robust array design. This is not only impacted by the velocity magnitude, but also the flow direction across the site. With inaccurate direction, an array optimized for wake avoidance may have the opposite effect in the near-mid wakes of turbines. Wakes should merge given enough distance, but the direction also plays an important role in assessing the environmental impact of an array on the surrounding natural environment and physical infrastructure. Hence, calibration data across the site is critical. Whilst vessel-mounted ADCP data are unlikely to provide a continuous record of sufficient duration for the current magnitude to be used in calibration, the principal axes of flow generally vary little with time. The methods used by Perez et al. (2023) could therefore be a critical aid in more cheaply ensuring that spatial variation in flow direction is correctly captured, to aid the array design process. As mentioned above, this could also include using the vessel mounted data for calibration, given that 3 flood/ebb cycles are sufficient for the purpose of calibrating the model.

Another consideration is the performance metrics imposed for modelling of array sites. In IEC TS 62600-201 (International Electrotechnical Commission, 2025), a maximum error of 5% (Cl. 7.5.3.1, Note 1) is recommended as a benchmark. However, this criterion is difficult to interpret in practice and, as noted in the standard (Cl. 7.5.3.1, Note 2), may be challenging to achieve in flows characterised by strong eddying behaviour. For example, the normalised RMSE for station 2013-ERI in the 2013 calibration (Figure 4) is approximately 5%–6%, marginally exceeding this threshold, with the uniform friction case exhibiting substantially larger errors due to over-amplification of the flow variability. While the mean absolute error is also recommended, reliance on a single bulk metric can be misleading. In particular, the distribution of error is important, as the inclusion of low flow speeds may bias aggregate statistics. Furthermore, asymmetric performance may not be captured by a single threshold; for instance, a model exhibiting a 2% error during flood tides and an 8% error during ebb tides may satisfy the overall criterion while still providing a poor representation of the flow dynamics. In addition to site-scale turbulent structures, measurement noise can introduce discrepancies that are not directly attributable to model deficiencies. Consequently, model development for scheme applications requires not only achieving nominal performance thresholds, but also the informed application and interpretation of data assimilation and diagnostic approaches, emphasising the critical role of modeller judgement in assessing and quantifying model skill.

At the time of writing, the MeyGen project has successfully bid for 59MW of capacity through Contracts for Difference. However, the lease allowance of 398MW is much larger. Not only do developers need to understand the intricacies of their site, but also the potential changes in flow influx as a result of introducing significant resistance to the channel. IEC TS 62600:201 states that ADCPs should be deployed at future turbine positions (Cl. 6.4.3.2) but, neighbouring sites may also change the influx into their site. Tables 4 and 5 show that even without the data included within the optimisation, the case calibrated for all of the Inner Sound data significantly outperforms a uniform or sedimentological approach. It should be noted that the model calibrated only for the Outer Sound (2001), performs extremely poorly for the Inner Sound, reflecting the difference in flow complexity between the two channels. Once all data is included within the calibration, the model can more accurately predict the velocity in both channels. Thus, this serves as an early indicator of the need for more strategic and distributed velocity data collection across all relevant channels for the marine spatial planners (in this case Crown Estate Scotland and the Marine Directorate), when assessing array-array impacts and understanding the limits on resource availability.

## 6. Conclusions

We consider the calibration of a regional-scale coastal ocean model using the bottom friction parameter, to reproduce the flow at a specific tidal site. Validation shows minimal sensitivity in elevation output whilst velocity magnitude and direction vary considerably. However, if calibration is limited to too few ADCPs, this can lead to misleading results, similar to relying only on tide gauge harmonic agreements. This is commonplace in tidal resource assessment studies, along with uniform parameterization of the bottom friction in 2D depth-averaged models. Uniform values of a friction coefficient, in this case Manning's $n_M$, were found to lead to good agreement in one tidal direction, but poor in the opposite. Good performance at multiple stations necessitates a spatially varying bottom friction distribution to accurately capture the spatio-temporal variation in velocity. The adjoint-based approach has successfully been applied for velocity sensor measurements, but overfitting was found when calibrating to the initial two monitor points; this was corrected when more calibration points were introduced. For resource assessment, incorrect initial assessments of yield could lead to overestimates in profitability that are challenging to recover for a developer. This is exacerbated by array design and environmental impact assessments being heavily dependent on accurate flow directions of the baseline resource model. Furthermore, disregard of model accuracy in neighboring channels could significantly impact the upper limit on resource assessment and array-array interactions. It is therefore paramount for developers and governing bodies to carry out strategic measurement campaigns to reduce the uncertainty in numerical models. In parallel, surveyors must take note of the need for accurate compass calibration and sensible ADCP frames to allow for accurate array design at site level. Final modeling will require an iterative process, as the optimal bottom friction distribution is mesh- and model-dependent.

## Appendix A: Coastal Ocean Model Calibration Techniques and Bottom Friction Representation

The simplest approach to calibration is to assume a uniform value for the bottom friction coefficient and enumerate through a range of parameters, until a minimal error is found between modeled and measured data (Davies & Aldridge, 1993). However, both skin friction and form drag will vary spatially (also, temporally) and therefore other studies have also enumerated through different parameters to determine the best coefficients for a variable friction representation. For example, Fernandes et al. (2001) presented an early study of the use of Telemac-2D in the Patos Lagoon, Brazil. There, they enumerated through uniform Manning, Chezy and Nikuradse friction representations before using a mapping between bed sediment and Nikuradse bottom friction. In that study, it was found that the variable representation improved reproduction of measurements. In the Bristol Channel, Mackie et al. (2021) similarly concluded that a variable representation based on the bed sediment particle size led to improved results over a uniform friction. Region-based approaches are also used. Athar et al. (2019) used a mapping based on segmenting the Persian Gulf and varying linear coefficients, such that the bed friction gradually increased from one side to the other. Mayo et al. (2014) apply regional splitting between basins in idealized and realistic cases, whereby a Kalman filter method is used to determine improved estimates. Warder et al. (2022) notes however, that the use of piecewise-constant bottom friction representation can be detrimental to model performance for tidal currents, where blockage like effects may be emulated by sharp discontinuities in bottom friction.

Rather than sedimentological or linear segmentation, various gradient-based methods for updating fields have instead relied on an "independent points scheme," whereby set nodes or bathymetric regions have their friction parameters varied and any intermediate points are estimated by interpolation (Lu & Zhang, 2006; Qian et al., 2021; Ullman & Wilson, 1998; Zhang et al., 2011). Allowing every node to be individually tuned would lead to substantial degrees of freedom and rapidly become untenable. Adjoint based methods, which determine the change in bed friction required to minimize the error, have also been used to investigate regions which necessitate further mesh resolution or parameter definition (Maßman, 2010) and for boundary forcing (Poncot et al., 2017). To circumvent the difficulty of calculating the derivative of the numerical model, Bayesian inversion can also be deployed (Warder et al., 2022). The study of Warder et al. (2020) compared the two, concluding that the suitable method depends on the input parameter space dimension, with the adjoint more mathematically appropriate when this exceeds four dimensions. Conversely, the Bayesian inference approach (via a Markov Chain Monte Carlo method) provides uncertainties in the resulting parameter estimates, which is beneficial in a domain where there is limited data available.

## Appendix B: Tidal Resource Assessment Validation

In tidal resource studies, ADCPs almost always feature as a reference for model accuracy, except in earlier studies where data was not yet available (Blunden & Bahaj, 2006; Karsten et al., 2008; Sutherland et al., 2007). Conversely, there is rarely discussion of model calibration, as the focus is typically on the demonstration of energy potential. Calibration or validation of the model is typically to one or two ADCPs in the region of interest where an array may be deployed (Carballo et al., 2009; Maslo et al., 2023; Ramos & Ringwood, 2016). These are sometimes limited to just several days (Chen et al., 2015; Fouz et al., 2022; Thiébaut & Sentchev, 2016; Xia et al., 2010) or are instead supported by vessel mounted (VM) ADCPs (Work et al., 2013), which can be challenging to accurately associate with the seabed mounted (SM) ADCPs due to calibration issues of the respective devices. VMADCPs are also limited by their timescales. Use of SMADCPs to extrapolate longer time series of VMADCPs is unproven and challenging, given that the spatiotemporal variation at energetic sites can be nonlinear (Warder et al., 2021).

At the Pentland Firth, a common case study location off the North East of mainland Scotland, 3 ADCPs were used for the studies of both Adcock et al. (2013) and O'Hara Murray and Gallego (2017). However, these were within the Outer Sound, whilst the actual development of MeyGen is within the Inner Sound. Nearby, at the Fall of Warness, Almoghayer et al. (2024) had 4 ADCPs to calibrate their modeling of turbines, but used only 1 to validate their ambient model. Other studies have also presented 3-6 ADCPs for validation of the model, however these are subsequently separated by several kilometres (Guerra et al., 2017; Hasegawa et al., 2011; Marta-Almeida et al., 2017; Mejia-Olivares et al., 2018; Park et al., 2019). One exception to the general rule is the Salish Sea, North America, where extensive ADCP work has been carried out (Polagye & Thomson, 2013; Yang et al., 2021). Due to the resource required for such a wide-scale measurement campaign, it is incredibly unusual to have such outstanding spatial coverage as in Yang et al. (2020), where the US Department of Energy funded 135 ADCP deployments. This has led to a 3D FVCOM model which can be used to “accurately characterize the tidal stream energy resource.” Several studies make similar claims, or inferences, that their model is sufficiently accurate for further use in resource assessment. However, both Yang et al. (2020) and Michelet et al. (2020) present comparisons to ADCPs where, although the velocity magnitude shows excellent agreement, the principal directions of the ebb and flood show notable discrepancy.

**Table B1**
*Selected Resource Assessment Studies in the Pentland Firth and Other Energetic Sites*

| Ref. | No. of ADCPs | Cal. method | Comment |
|---|---|---|---|
| Adcock et al. (2013) | 3* | Enumeration (uniform) | Depth-averaged 2D DG-ADCIRC model with uniform friction focussed on the Pentland Firth. Same model used for Draper et al. (2014). *Only the harmonics of the ADCPs were available. |
| Ramos and Ringwood (2016) | 2SM | None | Delft-3D model of the Orkney Islands focussed on Fall of Warness. The ADCPs used are from different time periods and are 1 km apart. No calibration presented. |
| O'Hara Murray and Gallego (2017) | 3SM + numerous VM | Enumeration (uniform) | 3D FVCOM model of the Orkney Islands. 3× SMADCPs and VMADCP transects across various channels around the Pentland Firth and Orkneys are presented. |
| De Dominicis et al. (2017, 2018) | None | None | 3D FVCOM model with no specific calibration performed as study focussed only on large scale impacts. |
| Almoghayer et al. (2024) | 4* | None | TELEMAC-3D model of Fall of Warness with spatially varying friction coefficient. *ADCPs right next to a turbine to monitor wakes. Only 1 ADCP is used to validate the ambient model. |
| Blunden and Bahaj (2006) | None | None | TELEMAC-2D model of Portland Bill. No discussion of bottom friction. Validation using tidal elevation measurements and tidal stream diamonds from Admiralty charts. |
| Willis et al. (2010) | None | None | 2D depth-averaged flow model of the Bristol Channel. Insufficient information surrounding any use of ADCPs or calibration. |
| Xia et al. (2010) | 2 | None | 2D depth-averaged flow model of the Severn Estuary (Bristol Channel). ADCP comparisons are over very short time periods. No discussion of bottom friction. |
| Serhadlıoğlu et al. (2013) | 1* | Enumeration (uniform) | 2D depth-averaged model of the Anglesey Skerries. *Unclear if it is an ADCP, or some manipulated data based on a different kind of gauge. Calibration not described, but likely to tide gauges and using enumeration of uniform friction. |
| Lewis et al. (2015) | None | None | ROMS 3D model of the Irish Sea. This was a large scale model, not a targeted study. No calibration presented. |
| Thiébaut and Sentchev (2016) | 2* | None | MARS-3D model of Dover Strait. *ADCPs were only 4 and 7 days, at different times. Also used Very High Frequency Radar (VHFR) which provides surface layer velocities at 20 min frequency. Model calibration details are provided in Jouanneau et al. (2013)—drag coefficient proportional to the local depth and the bed roughness—validated only, no calibration. |
| Fouz et al. (2022) | 2 | None | Delft-2DH model of Shannon Estuary (West of Ireland). ADCPs are 10/30 min resolution and recorded over different time periods, spaced far apart. One is only for 4 days. |
| Sutherland et al. (2007) | None | Enumeration | Depth-averaged TIDE-2D model of Johnstone Strait, Vancouver Island. Hints at calibration to tide gauges by changing the region based frictions. |
| Karsten et al. (2008) | None | Unknown | Depth-averaged FVCOM 2D model of Minas Passage, Bay of Fundy. Calibration and bottom friction not discussed. |
| Carballo et al. (2009) | 1 | Unknown | Delft3D-FLOW model (used in 2D mode) of Ría de Muros (NW Spain). Calibration and bottom friction not discussed. |
| Polagye and Thomson (2013) | 8 | N/A | No numerical model. Admiralty Inlet, Puget Sound, WA, USA |
| Hasegawa et al. (2011) | 3 | None | 3D Princeton Ocean Model of Bay of Fundy (BoF) and Gulf of Maine. No calibration, just validation. Also discusses that 2D models use bottom friction parameterization which is not suitable in BoF because of strong vertical variation. |
| Yang et al. (2013) | N/A | N/A | 3D FVCOM idealized model. |
| Work et al. (2013) | 1SM + 1VM | Unknown | 2D ROMS model (with a vertical profile applied to make it 3D) of Beaufort River, South Carolina, USA. Model is calibrated, but no description of how—most likely a uniform bottom friction that is enumerated. |
| Chen et al. (2015) | 2 | None | Delft-3D model of Zhaitang Island, Yellow Sea, China. ADCPs were measured for 1 day only. No discussion of bottom friction. |
| Guerra et al. (2017) | 6 | None | FVCOM model of Chacao Channel, Chile. ADCPs are spaced quite distantly (4–8 km apart) along the channel. No description of calibration or bed friction. |

**Table B1**
*Continued*

| Ref. | No. of ADCPs | Cal. method | Comment |
|---|---|---|---|
| Marta-Almeida et al. (2017) | 3* | None | 3D ROMS model of Baía de Todos os Santos, Brazil. *Data missing from all 3, so depth-averaged in the same region. Uniform roughness length. Model information in Marta-Almeida et al. (2019). |
| Mejia-Olivares et al. (2018) | 4 | None | TELEMAC-2D model of Gulf of California, Mexico. ADCPs are all fairly distant. |
| Park et al. (2019) | 1–4 | None | 2D MOHID model of Southwestern Sea of Korea. This was a large scale model, not a targeted study. No calibration presented. |
| Michelet et al. (2020) | 1 | None | 3D ROMS model of Fromveur Strait, off western Brittany. Sediment-based bed roughness values. |
| Garcia Novo and Kyozuka (2021) | None | None | 2D FVCOM model of Western Japan. This was a large scale model, not a targeted study. No calibration presented. |
| Yang et al. (2021) | 132 | None | 3D FVCOM model of the Salish Sea (including Puget Sound). ADCPs are over a large region—this is not a targeted study of any one particular location. Uniform bed friction, maximum grid resolution is 50 m. Validation information in Yang et al. (2020). |
| Maslo et al. (2023) | 2 | None | 3D ROMS model of Cozumel Channel, Mexico. Uniform bed roughness. |
| Alday and Lavidas (2024) | None | Uniform (enumeration) | 2D Thetis model of the Netherlands. This was a large scale model, not a targeted study. |

## Appendix C: ADCP Data Summary

Numerous ADCP deployments have been undertaken at the MeyGen site, which led to gradual improvement in data quality and acquisition procedure. Surveys prior to 2013 were typically unsuccessful due to difficulties with the harsh marine conditions. Table 2 lists subsequent ADCP surveys. In March 2013, two ADCPs were deployed by the Energy Research Institute (ERI) and the University of Exeter (EXE). However, in both cases, the frames that contain the ADCPs saw sensor movement that impacted the reliability of the data. Reflecting on the usability of this data, frame rotation should not generally impact the velocity magnitude, but the compass was unable to re-calibrate correctly and thus the corrections to the direction were made to re-align to the principal direction calculated prior to frame movement.

Further ADCPs were deployed in 2017 campaigns to understand the behavior of the flow close to the turbines, with a particular emphasis on turbulence behavior. This is described in detail in Coles et al. (2018). Some of these ADCPs were positioned downstream of turbines in one direction, and so are only to be used for one tide, as discussed in Table C1. A recent 2022 campaign deployed one further seabed mounted (SM) ADCP, coupled with vessel mounted (VM) ADCPs to investigate the available resource and behavior downstream of the turbines. Similar frame rotation issues occurred on the SMADCP, and the same approach as for the 2013 data is used.

In all cases, limited, if any, compass calibration was conducted. The anticipated accuracy of these compasses, *when calibrated correctly*, is around 4–5°. Using the VMADCP data for reference, regardless of compass error, indicates certain anomalies in principal flow directions for the SMADCPs. For example, ADCP2017-3 appears to be offset in the clockwise direction. Hence, we can make informed corrections to align the ADCPs based on vessel mounted ADCP surveys. These corrections are shown in Figure 6. There is a limit on the confidence of these corrections, as ultimately insufficient compass calibration work has been performed. This is discussed further in Section 5.

**Table C1**
*ADCP Data Summary*

| | ID | Start Date | End Date | Data interval [s] | Comments |
|---|---|---|---|---|---|
| Inner Sound | 2013-ERI | 17/02/2013 | 20/03/2013 | 1 | Short gaps in 1s data provided exist, which have been infilled with 10s data. Compass calibration carried out with ±4° error. Considerable frame movement causes error in the measured principal direction persistently after 5 days of data recording. This has been corrected based on the principal direction calculated pre-movement |
| | 2013-EXE | 19/02/2013 | 22/03/2013 | 1 | Considerable ADCP frame movement on 02/03/2013, causing a direction shift in the data thereon. This has been corrected using the principal directions calculated pre-movement |
| | 2017–2 | 03/08/2017 | 29/08/2017 | 0.5 | No known issues |
| | 2017–3 | 02/08/2017 | 29/08/2017 | 0.5 | Ebb data may be impacted by close proximity to Tidal Turbine Generator (TTG) 3. Flood results could be impacted by TTG1, though there is a distance of 175.6 m (9.8D) between the two of them, so the majority of wake recovery should have occurred by this point |
| | 2017–4 | 15/10/2017 | 12/12/2017 | 0.5 | Flood results may be impacted by interactions with upstream TTG1 and TTG2, though once again, these are sufficiently far apart that the influence should not be substantial. The ebb flow is not expected to be impacted |
| | 2022 | 20/10/2022 | 30/11/2022 | 600 | Data is only typically recorded up to ≈32 m above the seabed, whilst the depth is closer to 39 m. All observed values, once depth-averaged, may be underestimated. 10-minute sampling may suppress peak values. Due to known issues with the ADCP deployment, corrections are made to the direction before and after the 25th of November |
| Outer Sound | 2001-C1 | 15/09/2001 | 14/10/2001 | 600 | Speeds are provided at all bin depths. Directions are provided separately, at only 3 heights. Quality of data unknown and likely limited, so indicative only. Old data set obtained with moored bed ADCPs, so direction unlikely to be accurate |
| | 2001-C1 | 19/09/2001 | 20/10/2001 | | |
| | 2001-C1 | 18/09/2001 | 14/10/2001 | | |

## Appendix D: Spatial Regularization and Relationship With Sedimentology

Table 1 presented various studies performing calibration of control parameters, typically the friction field. The value of this field can vary spatially to regularize the optimisation problem, which can also accelerate convergence. Our hypothesis is that a uniform parameter that is commonly imposed across the domain is likely sub-optimal, whilst no regularization can lead to overfitting near observed data stations.

The key objective of this study is to investigate the sensitivity of the calibration process to the measured data coverage over a relatively small area of interest. To discern this, calibration was first conducted without any spatial regularization. Calibration was subsequently re-performed with both implicit and explicit regularization as described in the following sections, to indicate whether this impacts the results.

### D1. Hessian-Based Penalization

One method of preventing sharp changes in the control parameter is to supplement the cost function explicitly with a regularization term, $J_r(n_M)$,

$$J(\mathbf{Q}, n_M) = J_\sigma(\mathbf{Q}, n_M) + J_r(n_M) \tag{D1}$$

$$J_r(\boldsymbol{\theta}) = \alpha \|\mathcal{H}(n_M)(\Delta x)^2\|_2^2 = \alpha \int_\Omega \mathcal{H}(n_M) : \mathcal{H}(n_M)(\Delta x)^4 \, \mathrm{d}x, \tag{D2}$$

where $\mathcal{H}(n_M)$ denotes the Hessian of the Manning coefficient field with respect to the spatial coordinates, $\|\cdot\|_2$ is the $L_2$ norm, $\Delta x$ is the local mesh element size, and $\alpha$ is a regularization parameter.

Only the Hessian is penalized, that is, the constant part and first gradients of $n_M$ are not constrained at all. Detailed finite element implementation details of the Hessian regularization and explanation of the mathematical rigor of the method can be found in Appendix B of Kärnä et al. (2023). Scaling by the mesh element size promotes a smoother Manning coefficient field with higher variability permitted in regions of finer resolution.

**Table D1**
*Period Averaged Calibration Speed Rating and Principal Direction Discrepancy in Each Case for Hessian-Based Regularization for ADCP Deployments at the Inner Sound*

| | Average speed rating | | Average principal direction discrepancy (°) | |
|---|---|---|---|---|
| Calibration case | Flood | Ebb | Flood | Ebb |
| Uniform | 92.1 | 92.7 | 2.1 | 2.1 |
| 2013 | 92.9 | 92.9 | 0.5 | 1.2 |
| 2013/17a | 93.1 | 93.0 | 1.2 | 0.9 |
| 2013/17b | 93.0 | 93.1 | 1 | 0.9 |
| 2013/17/22 | 93.5 | 93.1 | 0.9 | 0.6 |

*Note.* Refer to Tables 4–7 for the main study equivalents.

The results are shown in Table D1. We present only the average results for brevity, showing similar trends found when regularization was not applied. The final mapping of Manning coefficient is shown in Figure D1, showing the smoothing effect of the regularization.

### D2. Independent Points Scheme

An alternative method that can more heavily enforce smoothness is to use an independent point scheme. Rather than explicitly penalize the cost function, a set of control points are specified. Between these points, an interpolation method is used to estimate the values. Similarly to the previous approach relying to $\Delta x$ in Hessian-based regularization, the density of control points can be increased areas of interest. This is applied here, with 500 m resolution in the main area of interest, 2.5 km resolution in the surrounding channels and 20 km resolution elsewhere.

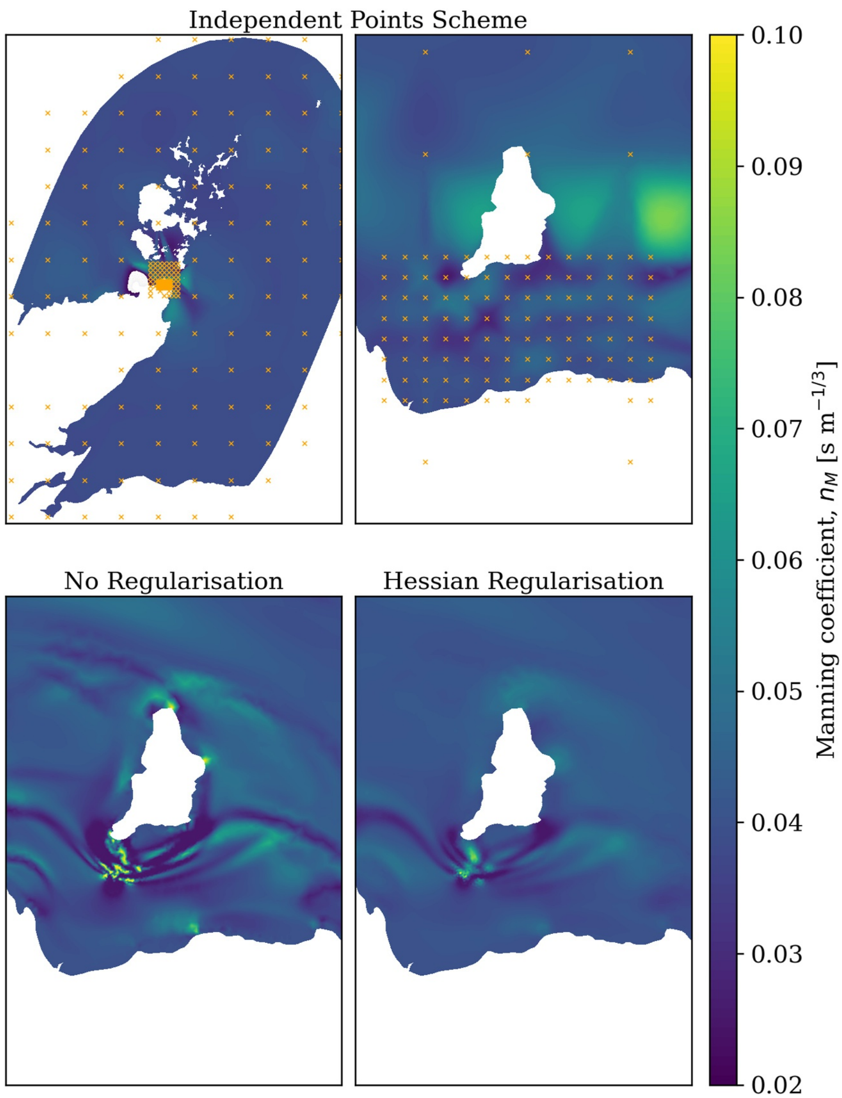


**Figure D1.** Results from applying different spatial regularization options in the calibration of the bottom friction. All Inner Sound data is used. Orange markers indicate the independents point used for interpolation in the IPS case. Projection: UTM Zone 30N.

**Table D2**
*Period Averaged Calibration Speed Rating and Principal Direction Discrepancy in Each Case for Independent Points Scheme Based Regularization for ADCP Deployments at the Inner Sound*

| | Average speed rating | | Average principal direction discrepancy (°) | |
|---|---|---|---|---|
| Calibration case | Flood | Ebb | Flood | Ebb |
| Uniform | 92.1 | 92.7 | 2.1 | 2.1 |
| 2013 | 93.0 | 94.2 | 1.0 | 1.2 |
| 2013/17a | 93.4 | 94.3 | 0.9 | 0.8 |
| 2013/17b | 93.4 | 94.1 | 0.7 | 1.2 |
| 2013/17/22 | 93.2 | 93.8 | 0.7 | 1.0 |

*Note.* Refer to Tables 4–7 for the main study equivalents.

The results are shown in Table D2. Similar trends are found again with respect to the main findings without regularization, but in the case with all Inner Sound data (2013/17/22), the optimisation converged early, potentially due to over-constraining the problem with so many ADCPs in such close proximity relative to the IPS grid spacing. This led to reduced performance relative to earlier cases where the 2022 data was not included.

## D3. Sedimentology

The sedimentological-based map is shown at regional-scale in Figure D2. This is compared to the adjoint output when calibrating against all ADCPs using Hessian-based penalization. With no data away from the Inner and Outer Sound, there are no changes to the rest of the domain as local upstream modifications are the most directly influential method of improving model agreement. Within the Inner Sound, even with Hessian based penalization, sharp local changes near the ADCP are generated as outlined in Section 4.3. The sediment-based map is derived from British Geological Society (2020), which is a very coarse map. However, using high resolution bathymetry various sand banks and ripples can be observed. As the bed shear stress term contains both the Manning coefficient and bathymetry, it is unsurprising to observe some similarity in patterns. Nonetheless, it can be observed that there is an increased friction off the south-west corner of Stroma, where we may have an under-resolved shallow bathymetric feature. Streaks of high and low friction can also be observed with the sand banks (e.g., in the east of the Inner Sound) and various locations with sharp changes between shallow and deeper bathymetry.

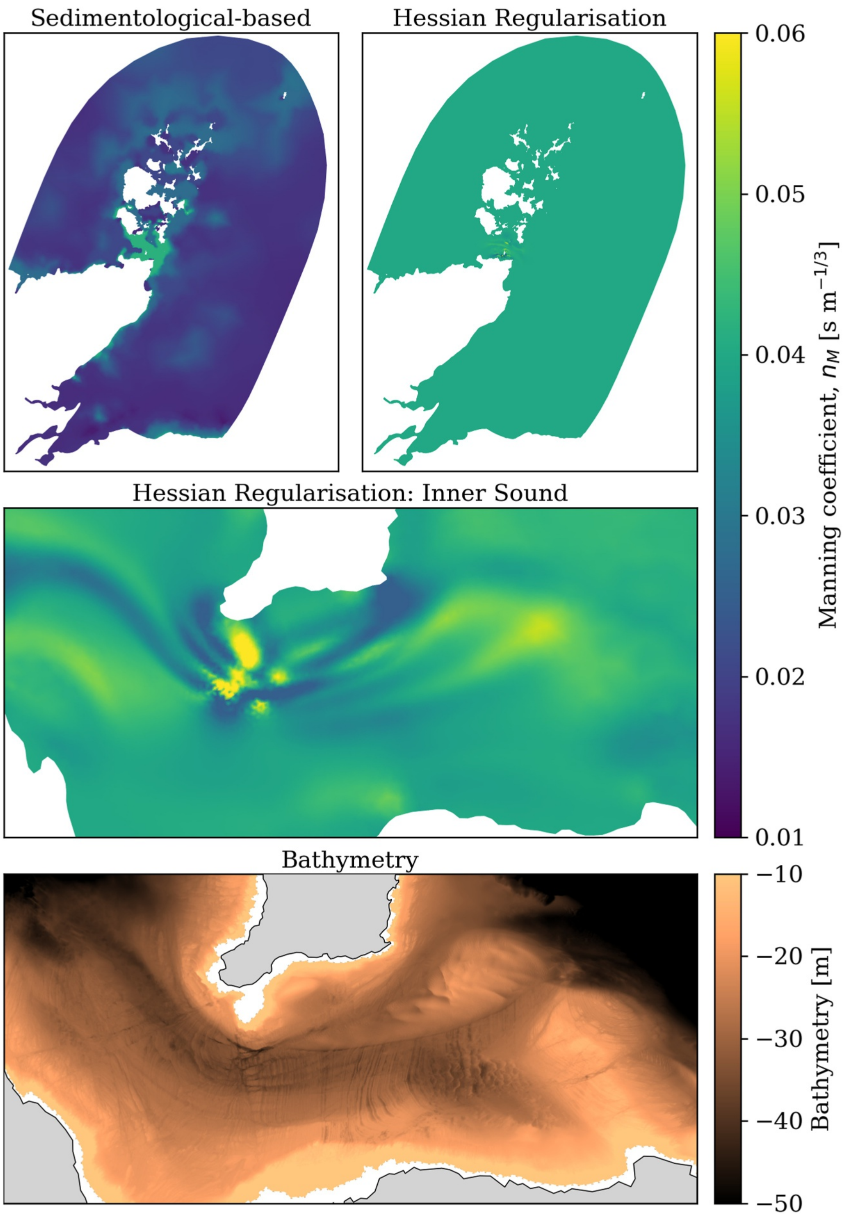


**Figure D2.** Top: Regional-scale comparison of sedimentological based friction to a Hessian penalized adjoint generated map. Middle: Hessian-based penalized adjoint generated map within the Inner Sound. Bottom: High resolution bathymetry data within the Inner Sound. Projection: UTM Zone 30N.

## Conflict of Interest

The authors declare no conflicts of interest relevant to this study.

## Availability Statement

The model source code is publicly available. The latest version of Firedrake, and its components, may be obtained from https://www.firedrakeproject.org; Thetis may be obtained from https://thetisproject.org/. The exact software versions used to produce the results in this paper have been archived on Zenodo (Zenodo/Firedrake, 2026; Zenodo/Thetis, 2026). The model configuration used to produce the presented results are also available on Zenodo (Zenodo/Model, 2026). Tidal forcing and inversion were computed with the Uptide Python package (Zenodo/Uptide, 2020).

Input data is cited in the paper and summarised as follows. Bathymetry data can be found on the Marine Data Exchange (IXSurvey Limited, 2025), Edina Digimap Service (2020) and GEBCO (2015). Forcing files can be obtained from TPXO (Egbert & Erofeeva, 2002).

This study uses ADCP data sets collected during multiple campaigns in the Pentland Firth. All data sets are commercially sensitive and subject to confidentiality restrictions imposed by MeyGen Ltd and project partners; therefore, they are not (currently) publicly available. The only current exception is the 2013-ERI data set, which is accessible via the Marine Data Exchange (Crown Estate Scotland, 2025).

- 2001 Outer Sound Campaign: Data is described in Easton et al. (2012).
- 2013 ERI/MeyGen Campaign: Data from the February–March 2013 deployment are described in the confidential report, Final Report for ADCP Deployment: Inner Sound, Pentland Firth (McIlvenny et al., 2013).
- 2017 MeyGen Campaign: A summary of this data set is published in Coles et al. (2018). The underlying data remain confidential.
- 2022 MeyGen Campaign: Data is detailed in the confidential report MeyGen 2 (Pentland Firth) ADCP Campaign Survey Report (Applied Renewables Research, 2023).

Access to these data sets and accompanying reports can be requested by submitting a formal data-sharing application to MeyGen Ltd (info@ampeak.energy). Approval is subject to MeyGen Ltd's data governance policy and may require execution of a non-disclosure agreement (NDA) and/or research collaboration agreement. These restrictions are necessary to protect commercially sensitive and proprietary information.

While the ADCP data sets used in this study cannot currently be made publicly available, researchers interested in similar investigations may refer to open-access data sets hosted by the UK Marine Data Exchange (https://www.marinedataexchange.co.uk/). These alternative data sets were not available at the time this study commenced. In addition, the data sets listed above are in the process of being uploaded on the site.

**Acknowledgments**

C. Jordan acknowledges the support of EPSRC, UK, through a PhD. studentship and the IAA PV182 ATARI project under grant agreement EP/X525698/1. A. Angeloudis acknowledges the support of the EC H2020 ILIAD DTO project under Grant 101037643 and EPSRC's CoTide Programme Grant (EP/X03903X/1). The authors would like to thank the authors of Farrell et al. (2013) and Kärnä et al. (2023) (amongst others) for the development of the inversion module tools that allowed for this work to be undertaken far more quickly than would have otherwise been possible. The authors would also like to thank Fraser Johnson and Gianlucca Gerich of MeyGen Ltd for provision of ADCP data. Finally, the authors would like to thank the reviewers for their constructive comments and insightful suggestions, which have helped to improve the clarity and quality of this manuscript.

## References

Adcock, T. A., Draper, S., Houlsby, G. T., Borthwick, A. G., & Serhadlioğlu, S. (2013). The available power from tidal stream turbines in the Pentland Firth. *Proceedings of the Royal Society A: Mathematical, Physical and Engineering Sciences*, *469*(2157), 20130072. https://doi.org/10.1098/rspa.2013.0072

Alday, M., & Lavidas, G. (2024). Assessing the tidal stream resource for energy extraction in The Netherlands. *Renewable Energy*, *220*, 119683. https://doi.org/10.1016/j.renene.2023.119683

Almoghayer, M. A., Lam, R., Sellar, B., Old, C., & Woolf, D. K. (2024). Validation of tidal turbine wake simulations using an open regional-scale 3D model against 1MW machine and site measurements. *Ocean Engineering*, *299*, 117402. https://doi.org/10.1016/j.oceaneng.2024.117402

Applied Renewables Research. (2023). *Meygen 2 (Pentland Firth) ADCP campaign survey report* (Technical Report). MeyGen Ltd. (Confidential document. Document No: MG-ADCP-230324-R-01-CB-A).

Athar, M. S., Ardalan, A. A., & Karimi, R. (2019). Hydrodynamic tidal model of the Persian Gulf based on spatially variable bed friction coefficient. *Marine Geodesy*, *42*(1), 25–45. https://doi.org/10.1080/01490419.2018.1527799

Avdis, A., Candy, A. S., Hill, J., Kramer, S. C., & Piggott, M. D. (2018). Efficient unstructured mesh generation for marine renewable energy applications. *Renewable Energy*, *116*, 842–856. https://doi.org/10.1016/j.renene.2017.09.058

Banerjee, T., Danilov, S., Klingbeil, K., & Campin, J.-M. (2024). Discrete variance decay analysis of spurious mixing. *Ocean Modelling*, *192*, 102460. https://doi.org/10.1016/j.ocemod.2024.102460

Blunden, L., & Bahaj, A. (2006). Initial evaluation of tidal stream energy resources at Portland Bill, UK. *Renewable Energy*, *31*(2), 121–132. (Marine Energy). https://doi.org/10.1016/j.renene.2005.08.016

British Geological Society. (2020). Seabed sediments 250K. Retrieved from https://www.bgs.ac.uk/datasets/marine-sediments-250k/

Byrd, R. H., Lu, P., Nocedal, J., & Zhu, C. (1995). A limited memory algorithm for bound constrained optimization. *SIAM Journal on Scientific Computing*, *16*(5), 1190–1208. https://doi.org/10.1137/0916069

Carballo, R., Iglesias, G., & Castro, A. (2009). Numerical model evaluation of tidal stream energy resources in the Ría de Muros (NW Spain). *Renewable Energy*, *34*(6), 1517–1524. https://doi.org/10.1016/j.renene.2008.10.028

Chen, Y., Lin, B., Lin, J., & Wang, S. (2015). Effects of stream turbine array configuration on tidal current energy extraction near an island. *Computers and Geosciences*, *77*, 20–28. https://doi.org/10.1016/j.cageo.2015.01.008

Coles, D., Greenwood, C., Vogler, A., Walsh, T., & Taaffe, D. (2018). Assessment of the turbulent flow upstream of the Meygen Phase 1A tidal stream turbines. In *Proceedings of the Asian wave and tidal energy conference, Taipei, Taiwan*.

Crown Estate Scotland. (2025). 2013, ERI, Meygen, inner sound, ADCP survey. (Marine Data Exchange dataset (CES-119). Data collected in 2013 by Environmental Research Institute (ERI) Retrieved from https://www.marinedataexchange.co.uk/details/CES-119/2013-eri-meygen-inner-sound-adcp-survey

Davies, A. M., & Aldridge, J. N. (1993). A numerical model study of parameters influencing tidal currents in the Irish Sea. *Journal of Geophysical Research*, *98*(C4), 7049–7067. https://doi.org/10.1029/92JC02890

De Dominicis, M., O'Hara Murray, R., & Wolf, J. (2017). Multi-scale ocean response to a large tidal stream turbine array. *Renewable Energy*, *114*, 1160–1179. https://doi.org/10.1016/j.renene.2017.07.058

De Dominicis, M., O'Hara Murray, R., & Wolf, J. (2018). Comparative effects of climate change and tidal stream energy extraction in a Shelf Sea. *Journal of Geophysical Research: Oceans*, *123*(7), 5041–5067. https://doi.org/10.1029/2018JC013832

Department for Energy Security and Net Zero. (2023). Contracts for difference (CfD) allocation round 5: Results. Retrieved from https://www.gov.uk/government/publications/contracts-for-difference-cfd-allocation-round-5-results
Draper, S., Adcock, T. A., Borthwick, A. G., & Houlsby, G. T. (2014). Estimate of the tidal stream power resource of the Pentland Firth. *Renewable Energy*, *63*, 650–657. https://doi.org/10.1016/j.renene.2013.10.015
Easton, M. C., Woolf, D. K., & Bowyer, P. A. (2012). The dynamics of an energetic tidal channel, the Pentland Firth, Scotland. *Continental Shelf Research*, *48*, 50–60. https://doi.org/10.1016/j.csr.2012.08.009
Edina Digimap Service. (2020). *Hydrospatial one, gridded bathymetry*. SeaZone Solutions Ltd. Retrieved from http://digimap.edina.ac.uk/marine/
Egbert, G. D., & Erofeeva, S. Y. (2002). Efficient inverse modeling of Barotropic Ocean tides. *Journal of Atmospheric and Oceanic Technology*, *19*(2), 183–204. https://doi.org/10.1175/1520-0426(2002)019<0183:EIMOBO>2.0.CO;2
Farrell, P. E., Ham, D. A., Funke, S. W., & Rognes, M. E. (2013). Automated derivation of the adjoint of high-level transient finite element programs. *SIAM Journal on Scientific Computing*, *35*(4), C369–C393. https://doi.org/10.1137/120873558
Fernandes, E. H., Dyer, K. R., & Niencheski, L. F. H. (2001). Calibration and validation of the TELEMAC-2D model to the Patos Lagoon (Brazil). *Journal of Coastal Research*, 470–488. Retrieved from http://www.jstor.org/stable/25736313
Fouz, D., Carballo, R., López, I., & Iglesias, G. (2022). Tidal stream energy potential in the Shannon Estuary. *Renewable Energy*, *185*, 61–74. https://doi.org/10.1016/j.renene.2021.12.055
Funke, S. (2013). *The automation of PDE-constrained optimisation and its applications* (Thesis or dissertation). Imperial College London. https://doi.org/10.25560/11079
Garcia Novo, P., & Kyozuka, Y. (2021). Tidal stream energy as a potential continuous power producer: A case study for West Japan. *Energy Conversion and Management*, *245*, 114533. https://doi.org/10.1016/j.enconman.2021.114533
Garrett, C., & Cummins, P. (2008). Limits to tidal current power. *Renewable Energy*, *33*(11), 2485–2490. https://doi.org/10.1016/j.renene.2008.02.009
GEBCO. (2015). GEBCO_2014 grid. (Global bathymetric grid at 30 arc-second resolution. Released in 2015 by the General Bathymetric Chart of the Oceans (GEBCO) under IHO-IOC) Retrieved from https://www.gebco.net/data-products/historical-data-sets#gebco_2014
Guerra, M., Cienfuegos, R., Thomson, J., & Suarez, L. (2017). Tidal energy resource characterization in Chacao Channel, Chile. *International Journal of Marine Energy*, *20*, 1–16. https://doi.org/10.1016/j.ijome.2017.11.002
Guillou, N., & Thiébot, J. (2016). The impact of seabed rock roughness on tidal stream power extraction. *Energy*, *112*, 762–773. https://doi.org/10.1016/j.energy.2016.06.053
Gunn, K., & Stock-Williams, C. (2013). On validating numerical hydrodynamic models of complex tidal flow. *International Journal of Marine Energy*, *3–4*, e82–e97. https://doi.org/10.1016/j.ijome.2013.11.013
Ham, D. A., Kelly, P. H. J., Mitchell, L., Cotter, C. J., Kirby, R. C., Sagiyama, K., et al. (2023). Firedrake user manual (First Edition) [Computer software manual]. https://doi.org/10.25561/104839
Hasegawa, D., Sheng, J., Greenberg, D. A., & Thompson, K. R. (2011). Far-field effects of tidal energy extraction in the Minas Passage on tidal circulation in the Bay of Fundy and Gulf of Maine using a nested-grid coastal circulation model. *Ocean Dynamics*, *61*(11), 1845–1868. https://doi.org/10.1007/s10236-011-0481-9
International Electrotechnical Commission. (2025). Marine energy. Wave, tidal and other water current converters—Tidal energy resource assessment and characterization (2.0 ed.). Technical Specification No. 62600-201:2025. 3 rue de Varembé, PO Box 131, CH-1211 Geneva 20, Switzerland: IEC.
IXSurvey Limited. (2025). 2009 inner sound, sound of stroma ixsurvey geophysical survey (ces-121). (Collection date: September 2009; published on Marine Data Exchange by Crown Estate Scotland in March 2025) Retrieved from https://www.marinedataexchange.co.uk/details/CES-121/2009-inner-sound-sound-of-stroma-ixsurvey-geophysical-survey
Jordan, C., & Angeloudis, A. (2025). Effects of bathymetric constraints in tidal stream array layout design. *Journal of Hydraulic Research*, *63*(5), 622–639. https://doi.org/10.1080/00221686.2025.2554989
Jordan, C., Coles, D., Johnson, F., & Angeloudis, A. (2023). On tidal array layout sensitivity to regional and device model representation. *Proceedings of the European Wave and Tidal Energy Conference* (Vol. 15). https://doi.org/10.36688/ewtec-2023-302
Jordan, C., Dundovic, D., Fragkou, A. K., Deskos, G., Coles, D. S., Piggott, M. D., & Angeloudis, A. (2022). Combining shallow-water and analytical wake models for tidal array micro-siting. *Journal of Ocean Engineering and Marine Energy*, *8*(2), 193–215. https://doi.org/10.1007/s40722-022-00225-2
Jouanneau, N., Sentchev, A., & Dumas, F. (2013). Numerical modelling of circulation and dispersion processes in Boulogne-sur-Mer harbour (Eastern English Channel): Sensitivity to physical forcing and harbour design. *Ocean Dynamics*, *63*(11–12), 1321–1340. https://doi.org/10.1007/s10236-013-0659-4
Kantha, L. H., & Clayson, C. A. (2000). *Numerical models of oceans and oceanic processes* (1st ed., Vol. 66). Elsevier. Retrieved from https://shop.elsevier.com/books/numerical-models-of-oceans-and-oceanic-processes/kantha/978-0-12-434068-8
Kärnä, T., Kramer, S. C., Mitchell, L., Ham, D. A., Piggott, M. D., & Baptista, A. M. (2018). Thetis coastal ocean model: Discontinuous Galerkin discretization for the three-dimensional hydrostatic equations. *Geoscientific Model Development Discussions (GMDD)*, *2018*, 1–36. https://doi.org/10.5194/gmd-2017-292
Kärnä, T., Wallwork, J. G., & Kramer, S. C. (2023). Efficient optimization of a regional water elevation model with an automatically generated adjoint. *Journal of Advances in Modeling Earth Systems*, *15*(10), e2022MS003169. https://doi.org/10.1029/2022MS003169
Karsten, R. H., McMillan, J. M., Lickley, M. J., & Haynes, R. D. (2008). Assessment of tidal current energy in the Minas Passage, Bay of Fundy. *Proceedings of the Institution of Mechanical Engineers, Part A: Journal of Power and Energy*, *222*(5), 493–507. https://doi.org/10.1243/09576509JPE555
Kirby, J. T. (2016). Boussinesq models and their application to coastal processes across a wide range of scales. *Journal of Waterway, Port, Coastal, and Ocean Engineering*, *142*(6), 03116005. https://doi.org/10.1061/(ASCE)WW.1943-5460.0000350
Lewis, M., Neill, S., Robins, P., & Hashemi, M. (2015). Resource assessment for future generations of tidal-stream energy arrays. *Energy*, *83*, 403–415. https://doi.org/10.1016/j.energy.2015.02.038
Lu, X., & Zhang, J. (2006). Numerical study on spatially varying bottom friction coefficient of a 2D tidal model with adjoint method. *Continental Shelf Research*, *26*(16), 1905–1923. https://doi.org/10.1016/j.csr.2006.06.007
Mackie, L., Evans, P. S., Harrold, M. J., O'Doherty, T., Piggott, M. D., & Angeloudis, A. (2021). Modelling an energetic tidal strait: Investigating implications of common numerical configuration choices. *Applied Ocean Research*, *108*, 102494. https://doi.org/10.1016/j.apor.2020.102494
Marta-Almeida, M., Cirano, M., Guedes Soares, C., & Lessa, G. C. (2017). A numerical tidal stream energy assessment study for Baía de Todos os Santos, Brazil. *Renewable Energy*, *107*, 271–287. https://doi.org/10.1016/j.renene.2017.01.047

Marta-Almeida, M., Lessa, G. C., Aguiar, A. L., Amorim, F. N., & Cirano, M. (2019). Realistic modelling of shelf-estuary regions. *Ocean Dynamics*, *69*(11–12), 1311–1331. https://doi.org/10.1007/s10236-019-01304-z

Maslo, A., Mariño-Tapia, I., Hernández, E. S., & Casarín, R. S. (2023). Modelling the impacts of a large marine turbine array in the Cozumel Channel. *Ocean Engineering*, *289*, 116153. https://doi.org/10.1016/j.oceaneng.2023.116153

Mayo, T., Butler, T., Dawson, C., & Hoteit, I. (2014). Data assimilation within the Advanced Circulation (ADCIRC) modeling framework for the estimation of Manning's friction coefficient. *Ocean Modelling*, *76*, 43–58. https://doi.org/10.1016/j.ocemod.2014.01.001

Maßman, S. (2010). Sensitivities of an adjoint, unstructured mesh, tidal model on the European Continental Shelf. *Ocean Dynamics*, *60*(6), 1463–1477. https://doi.org/10.1007/s10236-010-0347-6

McIlvenny, J., Dufaur, J., & Caljouw, R. (2013). *Final report for ADCP deployment: Inner sound, Pentland Firth* (Technical Report, Confidential report, not publicly available. Report Date: 15 August 2013. Deployment: 17 February–21 March 2013). Environmental Research Institute (ERI) and Meygen Ltd.

Mejia-Olivares, C. J., Haigh, I. D., Wells, N. C., Coles, D. S., Lewis, M. J., & Neill, S. P. (2018). Tidal-stream energy resource characterization for the Gulf of California, México. *Energy*, *156*, 481–491. https://doi.org/10.1016/j.energy.2018.04.074

Michelet, N., Guillou, N., Chapalain, G., Thiébot, J., Guillou, S., Goward Brown, A., & Neill, S. (2020). Three-dimensional modelling of turbine wake interactions at a tidal stream energy site. *Applied Ocean Research*, *95*, 102009. https://doi.org/10.1016/j.apor.2019.102009

Mitusch, S. K., Funke, S. W., & Dokken, J. S. (2019). dolfin-adjoint 2018.1: Automated adjoints for fenics and firedrake. *Journal of Open Source Software*, *4*(38), 1292. https://doi.org/10.21105/joss.01292

Monahan, T., Tang, T., & Adcock, T. A. (2023). A hybrid model for online short-term tidal energy forecasting. *Applied Ocean Research*, *137*, 103596. https://doi.org/10.1016/j.apor.2023.103596

O'Hara Murray, R., & Gallego, A. (2017). A modelling study of the tidal stream resource of the Pentland Firth, Scotland. *Renewable Energy*, *102*, 326–340. https://doi.org/10.1016/j.renene.2016.10.053

Ouda, M., & Toorman, E. A. (2019). Development of a new multiphase sediment transport model for free surface flows. *International Journal of Multiphase Flow*, *117*, 81–102. https://doi.org/10.1016/j.ijmultiphaseflow.2019.04.023

Park, J.-S., Lee, C.-Y., Park, J.-S., Choi, H.-W., Ko, D.-H., & Lee, J.-L. (2019). Assessment of tidal stream energy resources using a numerical model in Southwestern Sea of Korea. *Ocean Science Journal*, *54*(4), 529–541. https://doi.org/10.1007/s12601-019-0038-2

Perez, L., Droniou, E., Huchet, M., Johnson, F., baldock, A., & Boake, C. (2023). Resource assessment using a combination of seabed mounted and semi-stationary vessel-mounted ADCP measurements. *Proceedings of the European Wave and Tidal Energy Conference* (Vol. 15). https://doi.org/10.36688/ewtec-2023-457

Polagye, B., & Thomson, J. (2013). Tidal energy resource characterization: Methodology and field study in Admiralty Inlet, Puget Sound, WA (USA). *Proceedings of the Institution of Mechanical Engineers, Part A: Journal of Power and Energy*, *227*(3), 352–367. https://doi.org/10.1177/0957650912470081

Poncot, A., Goeury, C., Argaud, J.-P., Zaoui, F., Ata, R., & Audouin, Y. (2017). Optimal calibration of TELEMAC-2D models based on a data assimilation algorithm. In C. and Dorfmann & G. Zenz (Eds.), *Proceedings of the XXIVth telemac-mascaret user conference, 17 to 20 October 2017, Graz University of Technology, Austria* (pp. 73–80). Graz University of Technology. Retrieved from https://hdl.handle.net/20.500.11970/104487

Pugh, D., & Woodworth, P. (2014). *Sea level science: Understanding tides, surges, tsunamis and mean sea-level changes*. Cambridge University Press.

Qian, S., Wang, D., Zhang, J., & Li, C. (2021). Adjoint estimation and interpretation of spatially varying bottom friction coefficients of the M2 tide for a tidal model in the Bohai, Yellow and East China Seas with multi-mission satellite observations. *Ocean Modelling*, *161*, 101783. https://doi.org/10.1016/j.ocemod.2021.101783

Ramos, V., & Ringwood, J. V. (2016). Implementation and evaluation of the International Electrotechnical Commission specification for tidal stream energy resource assessment: A case study. *Energy Conversion and Management*, *127*, 66–79. https://doi.org/10.1016/j.enconman.2016.08.078

Rathgeber, F., Ham, D. A., Mitchell, L., Lange, M., Luporini, F., Mcrae, A. T. T., et al. (2016). Firedrake: Automating the finite element method by composing abstractions. *ACM Transactions on Mathematical Software*, *43*(3), 24:1–24:27. https://doi.org/10.1145/2998441

Sauvaget, P., David, E., & Guedes Soares, C. (2000). Modelling tidal currents on the coast of Portugal. *Coastal Engineering*, *40*(4), 393–409. https://doi.org/10.1016/S0378-3839(00)00020-X

Sellar, B. G., Wakelam, G., Sutherland, D. R., Ingram, D. M., & Venugopal, V. (2018). Characterisation of tidal flows at the European Marine Energy Centre in the absence of ocean waves. *Energies*, *11*(1), 176. https://doi.org/10.3390/en11010176

Serhadlıoğlu, S., Adcock, T. A., Houlsby, G. T., Draper, S., & Borthwick, A. G. (2013). Tidal stream energy resource assessment of the Anglesey Skerries. *International Journal of Marine Energy*, *3–4*, e98–e111. (Special Issue – Selected Papers—EWTEC2013). https://doi.org/10.1016/j.ijome.2013.11.014

Strickler, A. (1923). *Contributions to the question of a velocity formula and roughness data for streams, channels and closed pipelines* (Technical Report No. Mitteilung 16). Amt für Wasserwirtschaft.

Sutherland, G., Foreman, M., & Garrett, C. (2007). Tidal current energy assessment for Johnstone Strait, Vancouver Island. *Proceedings of the Institution of Mechanical Engineers, Part A: Journal of Power and Energy*, *221*(2), 147–157. https://doi.org/10.1243/09576509JPE338

Thiébaut, M., & Sentchev, A. (2016). Tidal stream resource assessment in the Dover Strait (eastern English Channel). *International Journal of Marine Energy*, *16*, 262–278. https://doi.org/10.1016/j.ijome.2016.08.004

Thiébot, J., Goeury, C., Travert, J.-P., Sebastian, A., & Salomon, J. (2026). The contribution of sensitivity analysis and data assimilation to tidal-stream resource assessment: The example of the Alderney race. *Applied Ocean Research*, *168*, 104970. https://doi.org/10.1016/j.apor.2026.104970

Ullman, D. S., & Wilson, R. E. (1998). Model parameter estimation from data assimilation modeling: Temporal and spatial variability of the bottom drag coefficient. *Journal of Geophysical Research*, *103*(C3), 5531–5549. https://doi.org/10.1029/97JC03178

Vennell, R., Funke, S. W., Draper, S., Stevens, C., & Divett, T. (2015). Designing large arrays of tidal turbines: A synthesis and review. *Renewable and Sustainable Energy Reviews*, *41*, 454–472. https://doi.org/10.1016/j.rser.2014.08.022

Virtanen, P., Gommers, R., Oliphant, T. E., Haberland, M., Reddy, T., Cournapeau, D., et al. (2020). SciPy 1.0: Fundamental algorithms for scientific computing in python. *Nature Methods*, *17*(3), 261–272. https://doi.org/10.1038/s41592-019-0686-2

Wang, D., Zhang, J., & Wang, Y. P. (2021). Estimation of bottom friction coefficient in multi-constituent tidal models using the adjoint method: Temporal variations and spatial distributions. *Journal of Geophysical Research: Oceans*, *126*(5), e2020JC016949. https://doi.org/10.1029/2020JC016949

Wang, X., Verlaan, M., Veenstra, J., & Lin, H. X. (2022). Data-assimilation-based parameter estimation of bathymetry and bottom friction coefficient to improve coastal accuracy in a global tide model. *Ocean Science*, *18*(3), 881–904. https://doi.org/10.5194/os-18-881-2022

Warder, S. C., Angeloudis, A., Kramer, S. C., Cotter, C. J., & Piggott, M. D. (2020). A comparison of Bayesian inference and gradient-based approaches for friction parameter estimation. *(Preprint on Earth ArXiv)*. https://doi.org/10.31223/osf.io/mv9qy

Warder, S. C., Angeloudis, A., & Piggott, M. D. (2022). Sedimentological data-driven bottom friction parameter estimation in modelling Bristol Channel tidal dynamics. *Ocean Dynamics*, *72*(6), 361–382. https://doi.org/10.1007/s10236-022-01507-x

Warder, S. C., Kramer, S. C., & Piggott, M. D. (2021). Non-deterministic effects in modelling the tidal currents in a high-energy coastal site. *(Preprint on Earth ArXiv)*. https://doi.org/10.31223/X55G7F

Warder, S. C., & Piggott, M. D. (2022). Optimal experiment design for a bottom friction parameter estimation problem. *GEM - International Journal on Geomathematics*, *13*(7), 361–382. https://doi.org/10.1007/s13137-022-00196-4

Willis, M., Masters, I., Thomas, S., Gallie, R., Loman, J., Cook, A., et al. (2010). Tidal turbine deployment in the Bristol channel: A case study. *Proceedings of the Institution of Civil Engineers: Energy*, *163*(3), 93–105. https://doi.org/10.1680/ener.2010.163.3.93

Work, P. A., Haas, K. A., Defne, Z., & Gay, T. (2013). Tidal stream energy site assessment via three-dimensional model and measurements. *Applied Energy*, *102*, 510–519. (Special Issue on Advances in sustainable biofuel production and use—XIX International Symposium on Alcohol Fuels—ISAF). https://doi.org/10.1016/j.apenergy.2012.08.040

Xia, J., Falconer, R. A., & Lin, B. (2010). Numerical model assessment of tidal stream energy resources in the severn Estuary, UK. *Proceedings of the Institution of Mechanical Engineers, Part A: Journal of Power and Energy*, *224*(7), 969–983. https://doi.org/10.1243/09576509JPE938

Yang, Z., Wang, T., Branch, R., & Xiao, Z. (2020). *Validation of the high-resolution Salish Sea tidal hydrodynamic model* (Technical Report No. PNNL-30448). Pacific Northwest National Laboratory.

Yang, Z., Wang, T., Branch, R., Xiao, Z., & Deb, M. (2021). Tidal stream energy resource characterization in the Salish Sea. *Renewable Energy*, *172*, 188–208. https://doi.org/10.1016/j.renene.2021.03.028

Yang, Z., Wang, T., & Copping, A. E. (2013). Modeling tidal stream energy extraction and its effects on transport processes in a tidal channel and bay system using a three-dimensional coastal ocean model. *Renewable Energy*, *50*, 605–613. https://doi.org/10.1016/j.renene.2012.07.024

Zenodo/Firedrake. (2026). Software used in “Assimilation of velocity data for tidal hydrodynamics model calibration”. https://doi.org/10.5281/zenodo.19551323

Zenodo/Model. (2026). *Thetis Inner Sound adjoint calibration simulation: Model*. Zenodo. https://doi.org/10.5281/zenodo.19606827

Zenodo/Thetis. (2026). *Thetis coastal ocean model source code*. Zenodo. (Currently awaiting sync, corresponds to Thetis_20240725 release on GitHub.). https://doi.org/10.5281/zenodo.20141672

Zenodo/Uptide. (2020). *First release of uptide v1.0*. Zenodo. https://doi.org/10.5281/zenodo.3909651

Zhang, J., Lu, X., Wang, P., & Wang, Y. P. (2011). Study on linear and nonlinear bottom friction parameterizations for regional tidal models using data assimilation. *Continental Shelf Research*, *31*(6), 555–573. https://doi.org/10.1016/j.csr.2010.12.011